Stress localisation in lamellar cementite and ferrite during elastoplastic deformation of pearlitic steel studied using diffraction and modelling

E. Gadalinska, A. Baczmanski, Chedly Braham, G. Gonzalez, H. Sidhom, S. Wronski, T. Buslaps, K. Wierzbanowski

International Journal of Plasticity 127 (2020) 102651

Contents lists available at ScienceDirect

International Journal of Plasticity

journal homepage: http://www.elsevier.com/locate/ijplas

Stress localisation in lamellar cementite and ferrite during elastoplastic deformation of pearlitic steel studied using diffraction and modelling

E. Gadalińska [a], A. Baczmański [b,*], C. Braham [c], G. Gonzalez [d], H. Sidhom [e], S. Wroński [b], T. Buslaps [f], K. Wierzbanowski [b]

[a] Łukasiewicz Research Network – Institute of Aviation, Materials and Structures Research Center, Al. Krakowska 110/114, 02-256, Warszawa, Poland
[b] AGH-University of Science and Technology, Faculty of Physics and Applied Computer Science, Al. Mickiewicza 30, 30-059, Kraków, Poland
[c] Laboratoire Procédés et Ingénierie en Mécanique et Matériaux, CRNS UMR 8006, Arts et Métiers-ParisTech, 151 Bd de L'Hôpital, 75013, Paris, France
[d] Instituto de Investigaciones en Materiales, Universidad Nacional Autónoma de México, Circuito Exterior S/N, Cd. Universitaria, A.P. 70-360, Coyoacán, C.P. 04510, Mexico
[e] Mechanical, Materials and Processes Laboratory (LR99ES05), ESSTT, 5, Avenue Taha Hussein 1008, University of Tunis, Tunisia
[f] ESRF, 6, Rue J. Horowitz, 38500, Grenoble Cedex, France

ARTICLE INFO

Keywords:
Pearlitic steel
Synchrotron diffraction
Self-consistent model
Stress localisation
Elastoplastic deformation

ABSTRACT

Synchrotron X-ray diffraction was applied to study the evolution of lattice strain and stresses in both phases of pearlitic steel during a tensile test. The advantage of the methodology used in this work is the possibility of experimental study of stress localisation, which is directly determined from measurements and can be used to study the process of strain strengthening of lamellar pearlite. It was found that in the elastic range of deformation, both cementite and ferrite are loaded similarly due to the nearly equal elastic properties of both phases, while plastic deformation leads to significant load transfer from ferrite to cementite. Due to the complexity of the lamellar microstructure of the material, the classical elastic-plastic self-consistent model does not correctly predict the partitioning of the stresses between phases during plastic deformation. Therefore, the grain-matrix interaction given by the self-consistent model was modified and successfully applied to simulate the interaction between phases.

The synchrotron experiment allowed us to determine the critical resolved shear stresses of ferrite phase in the pearlitic steel subjected to different thermal treatments. The role of cementite in material strengthening was evaluated on the basis of the evolution of von Mises stress, experimentally determined in both phases. It was found that during plastic deformations, the von Mises stress does not change significantly in ferrite compared to an important increase in elastically deformed cementite. Therefore, the partitioning of stresses between phases is mainly responsible for the strain strengthening of the tested pearlitic steel exhibiting fully lamellar microstructure.

* Corresponding author.
E-mail address: andrzej.baczmanski@fis.agh.edu.pl (A. Baczmański).

https://doi.org/10.1016/j.ijplas.2019.102651
Received 2 July 2019; Received in revised form 9 December 2019; Accepted 17 December 2019
Available online 28 December 2019

1. Introduction

Abbreviations

CRSS	critical resolved shear stress
EPSC	elastic-plastic self-consistent model
EPM	elastic-plastic mixed model
GND	geometrically necessary dislocation
H–P	Hall-Peach relation
L-C	Langford-Cohen relation
SEM	scanning electron microscope
SSD	statistically stored dislocation
TEM	transmission electron microscope
UTS	ultimate tensile stress
FEM	finite element method

Carbon steels are widely used in industrial applications due to their low cost and excellent combination of ductility and strength resulting from heat treatment (Das, 2018; Xiang et al., 2019; Yahyaoui et al., 2014) which can be significantly improved by processing, such as cold drawing (Lamontagne et al., 2015; Wei et al., 2019; Zhang et al., 2018). The yield stress of these steels varies with their carbon content from 450 MPa (0.4 wt% C) to 720 MPa (1.6 wt% C) and for a heavily drawn 0.88 wt% C steel up to 2400 MPa. The same trend was observed for the ultimate tensile stress (UTS), which varies from 700 to 1300 MPa and for the ductility varying from 3% to 12% (Young et al., 2007). Currently produced steel wires can reach a strength of up to 5 GPa (Wei et al., 2019) or even 6.8 GPa (Li et al., 2014). The fully pearlitic steel, with a carbon content near to 0.8 wt% C, is the most used in manufacturing plain carbon steel to produce wires for reinforcing tires, cables for suspension bridges, engineering springs for automotive and railroads. The structure of this steel consists of cementite granules or alternating parallel lamellae of cementite, forming randomly orientated colonies of pearlite. Cementite, considered as a hard phase, contributes to the strength of pearlite, while the soft ferrite matrix provides ductile properties. Several studies have been devoted to microstructure investigation at different length scales and its effect on the behaviour under loading up to fracture (Sidhom et al., 2015; Zhao et al., 2018). Also the influence of fatigue tests (Adamczyk-Cieślak et al., 2019; Leitner et al., 2019), cold rolling (Liu et al., 2018) and cold drawing (Das, 2018; Zhang et al., 2018) on mechanical properties and microstructure of pearlite was investigated. A significant role of interfacial dislocation in deformation and fracture processes in nanolayered composite materials was recently demonstrated using molecular dynamics calculation (Shimokawa et al., 2019). It was found that the mechanical properties and the elastoplastic behaviour of these steels are controlled by numerous microstructural variables such as prior austenite grain size, pearlite colonies orientation and size, cementite morphology, inter-lamellar spacing, interfacial deformation and fracture.

Direct observations performed using TEM (Fang et al., 2014) and synchrotron diffraction method (Taniyama et al., 2017) showed the evolution of crystal lattice defects and the increase of dislocation density in cementite during severe plastic deformation of pearlite. However, in the latter study, the evolution of dislocation density was determined from a variation of diffraction peak widths, which may also result from other reasons. For example, Weisser et al. (2015) measured a large broadening of peaks for cementite using synchrotron radiation during a tensile test. They explained that this phenomenon is due to a significant local stress heterogeneity in cementite particles rather than due to the increase of dislocation density in this phase. Therefore, the authors suggested that the main contribution to peak broadening for cementite is related to pure elastic effects, whereas the peak broadening for ferrite was attributed to an increase in dislocation density.

Although the cementite is usually considered as purely elastic, the plastic/inelastic deformation of this phase was also observed during severe deformation of pearlitic steel, for example due to wire drawing. The EBSD and SEM investigations showed such phenomena as slipping and thinning of lamellae, as well as cementite fragmentation (Zhang et al., 2018). The latter processes usually lead to fracture and cracking processes initiated in the pearlite grains (Sidhom et al., 2015; Zhao et al., 2018). Using an *in situ* SEM method during tensile tests, the shearing and shear cracking across whole pearlite colonies of cementite lamellae were observed by Sidhom et al. (2015) for the last stage of deformation. The important evolution of the lamellar structure in pearlitic steel (0.8 wt% C) during the drawing process was described by Zhang et al. (2018), showing an aligning of the lamellae along the drawing directions for large deformations. Finally, it should be emphasised that during cold drawing process, a solid solution hardening mechanism related to the decomposition of cementite also occurs (Lamontagne et al., 2015; Liu et al., 2018; Zhang et al., 2018). All the mentioned processes lead to a complex evolution of the strengthening of the material during deformation.

It is generally recognised that the combined effects of ferrite hardness and stress partitioning between ferrite and cementite are the most important phenomena responsible for controlling the deformation, hardening and damage of pearlite. The initial yield stress of this steel is controlled mostly by the hardness of the ferrite and depends on different additive components (Iza-Mendia and Gutiérrez, 2013; Liu et al., 2018; Zhang et al., 2018), i.e.: the lattice friction stress, the interstitial and substitutional elements, contribution of the precipitates (solid solution hardening), the distance between cementite lamellae or/and ferrite grain size (boundary strengthening), the dislocation density and their special distribution in the ferrite (dislocation strengthening). The grain boundary strengthening is

caused by a pile-up of dislocations at the grain boundary, and consequently an increase of the stress necessary for slip initiation can be observed. The classical Hall-Peach (H–P) law says that the boundary strengthening contribution to the yield stress is proportional to the inverse square root of the grain size. This law was also used for pearlitic steel by Embury and Fisher (1966). In that work, the TEM experiment showed an important role of narrow, oriented dislocation cells in strengthening of drawn hypereutectoid steel (0.93 wt% C) wires. Using the H–P relation, the yield stress determined for drawn pearlite wires was correlated with wire diameter and the inter-lamellar spacings limiting dislocation gliding distance in ferrite. Different microstructures of C–Mn–Nb steel (ferrite–pearlite, bainite, quenched and tempered) were tested by Iza-Mendia and Gutiérrez (2013) in order to establish the empirical equations for calculation of the material yield stress. As the result the coefficient of H–P relation was found and moreover the strengthening effects coming from the Nb precipitation, free interstitial solutes and transformation dislocations were determined.

Although the H–P relation is frequently used to correlate strengthening due to grain or interphase boundaries, it seems incorrect in the case of fully pearlitic steel having lamellar microstructure. It was found that negative or too low values of the lattice friction stress were obtained when the H–P law was adjusted to experimental data (when the inter-lamellar spacing was considered as the grain size). Therefore a more appropriate relation is that in which the lamellar strengthening is proportional to the inverse of the distances between cementite lamella (Dollar et al., 1988; Marder and Bramfitt, 1976; Yahyaoui et al., 2014). This relation (L-C law) was proposed by Langford and Cohen (1969) and it is based on the Frank–Read mechanism of dislocation generation in ferrite lamellae (Li et al., 2003; Yahyaoui et al., 2014).

The Voce type law with L-C relation, describing both the initial yield stress and the strain hardening during plastic deformation, was proposed for fully lamellar pearlite (Allain and Bouaziz, 2008; Bouaziz and Le Corre, 2003). This empirical equation with adjustable parameters expresses the current yield stress σ^{per} as a superposition of the initial one (the first and second term) and the contribution depending on a current plastic strain ε^{per} of the sample, i.e.:

$$\sigma^{per}(\varepsilon^{per}) = \sigma_f^{per} + \frac{\mu M b}{s} + \frac{K}{g}\left[1 - exp\left(\frac{g}{2}\,\varepsilon^{per}\right)\right] \tag{1}$$

where: M is the mean Taylor factor, μ is the shear modulus of the ferrite, b is the Burgers' vector of mobile dislocations, s is the distance between cementite lamellas (inter-lamellar spacing), σ_f^{per} is the total friction stress (lattice strength increased by solid solution hardening), g and K are two calibrating parameters independent of the inter-lamellar spacing and chemical composition.

The above equation was used to predict the strengthening of fully pearlitic steels with different inter-lamellar spacings and for ferrite-pearlite steels containing different fractions of pearlite (Allain and Bouaziz, 2008). In the cases of ferrite, it was assumed that the grain size effect described by the H–P relation dominates and the interactions between dislocations can be neglected. Using the simplified stress localisation method the predicted stress-strain plots were successfully adjusted to the experimentally determined macroscopic behaviour of the studied material. Using the model, it was also shown that important internal stresses inside pearlite, as well as the plastic mismatch stresses between ferrite and pearlite, are generated during plastic deformation. These stresses arise due to the different mechanical behaviour of the phases (in this case ferrite and pearlite) and they are responsible for the significant kinematic hardening determined by Bauschinger tests for ferrite-pearlite, as well as for fully pearlitic steels. Important differences between stresses localised in ferrite and pearlite grains during the deformation process were found using model calculations. However, the presented model, based on Eq. (1), cannot predict the stress localisation in cementite and ferrite lamella within pearlite grains.

Recently, the Bouaziz's relation was successfully tested for C70 pearlitic steel which is studied also in the present work, showing a huge difference in the hardening process between a fully lamellar ($s = 206$ nm) and a globular microstructure (Allain et al., 2019). Therefore, it can be stated that the microstructure and especially the spatial arrangement of the cementite phase plays an important role in pearlite strengthening.

An important conclusion concerning the strain hardening of fully pearlitic steel with lamellar microstructure was drawn by Allain and Bouaziz (2008). They found that the distance between cementite lamella affects the initial yield (due to second terms of Eq. (1)) accordingly to L-C law but surprisingly it does not affect the strain-dependent term (third term of Eq. (1)). This result is fully supported by experimental results obtained for a wide range of interlamelar spacings ($s = 2$ nm–530 nm), as observed by many authors (Allain and Bouaziz, 2008; Dollar et al., 1988; Yahyaoui et al., 2014). The above conclusion leads to a deeper reflection on the nature of lamellar pearlite strengthening. If the main reason for strengthening is in the evolution of dislocation density and their spatial distribution, the width of the ferrite lamellae should affect the strengthening rate. This particularly applies to the plastically deformed ferrite lamellae adjacent to elastically deformed cementite. In the plastically deformed phase, the density of the so-called statistically stored dislocations (SSDs) increases, and moreover dislocation pile-ups against interphase boundaries. In addition, the accommodation of strain gradients between a hard cementite phase and a soft ferrite phase requires the generation of so-called geometrically necessary dislocations (GNDs) heterogeneously distributed in ferrite lamella (Linz et al., 2018; Zhang et al., 2013). It can be concluded that the varying density of dislocations and their heterogeneous distribution should lead to a significant dependence of the strengthening process on the width of the ferrite lamellae, but this is not the case observed in the experiment. Therefore, it is important to examine whether the process of strengthening of lamellar pearlite is dominated by the dislocation hardening of ferrite, whether it is mainly caused by stress partitioning between the cementite and ferrite phases during the plastic deformations process.

Using TEM and EBSD methods, the stress field in hypereutectoid lamellar pearlitic steel (0.9 wt% C) steel was investigated on the basis of crystallographic orientations of ferrite and cementite lattice. The material was subjected to isothermal heat treatment at 973 K for 900 s followed by water quenching (Nakada et al., 2009). It was found that the orientations of ferrite and cementite rotate simultaneously and the misorientation of the ferrite phase increases continuously through a cementite lamella. The TEM investigation did not show significant density of GNDs in the studied ferrite crystals, therefore only elastic strain was considered while possible

plastic rotation was neglected. Because lattice strain varies continuously between ferrite and cementite, it was concluded that variation of short-range local strain or lattice misfit at the ferrite-cementite interface was not responsible for the observed lattice rotation. Using a simple elastic model it was found that the stress change through cementite and ferrite lamella equals 380 and 63 MPa, respectively. The reason for this stress as well the range of variation was not discussed but it seems that the determined stress would be caused by hypereutectoid cementite or/and temperature gradients during sample quenching. Therefore, the range of stress variation is probably close to the size of pearlite grain or much longer. An important message of this paper is that the stress between ferrite and cementite within pearlite grain is not observed in spite of longer-range stress gradients which were found in the quickly cooled hypereutectoid lamellar pearlitic steel.

Two methodologies were developed in order to determine stresses in both phases of pearlitic steel during elastic and plastic deformation. The first one is based on the modelling, which relates the stress applied to the material with the stresses localised in the polycrystalline grains. To do this, the FEM calculations or/and crystallographic scale transition models can be used. Another methodology is a direct diffraction measurement of the elastic lattice strains (or stresses) localised in polycrystalline grains during elastic-plastic deformation. In this case, neutron or X-ray synchrotron radiation is usually applied.

Different crystallographic scale transition models were elaborated in order to predict micromechanical behaviour of one or two phase polycrystalline materials. Among them, the algorithms developed by Turner and Tomé (1994), Beyerlein and Tomé, (2008), Neil et al. (2010), Lebensohn et al. (2012), Upadhyay et al. (2018), Chelladurai et al. (2019) were used and their results were successfully compared with neutron and synchrotron diffraction experiments (e.g. Agnew et al., 2018; Cai et al., 2012; Jia et al., 2009; Neil et al., 2010). In parallel, the self-consistent crystallographic models were elaborated by Lipinski and Berveiller (1989), Lipinski et al. (1995), Bonfoh et al. (2004), Franz et al. (2013), Baczmański et al. (2016), Fajoui et al. (2016) and applied to interpret diffraction experiments (e.g. Baczmański et al., 2016; Gadalińska et al., 2018; Gloaguen et al., 2014; Hounkpati et al., 2016; Kot et al., 2019).

Experimental studies of mechanical properties of phases in the pearlitic and high carbon steels (containing cementite) were previously performed using *in situ* neutron diffraction (Daymond and Priesmeyer, 2002; Oliver et al., 2004) and synchrotron diffraction (Ghosh et al., 2018; Taupin et al., 2013; Young et al., 2007) for samples subjected to external loading. Analysing lattice strains in both phases an important stress transfer from plastically deformed ferrite to elastic cementite was found, i.e. the important reason for material strengthening was directly observed.

A successful prediction of the stress partitioning between ferrite and cementite (hypereutectoid structure) was done for the first time by Daymond and Priesmeyer (2002) using Elastic-Plastic Self-Consistent model (EPSC), based on the Eshelby inclusion method (Eshelby, 2007). In this aim, the EPSC model developed by Turner and Tomé (1994) was modified to take into account the presence of elastic cementite phase. The model results were compared with neutron diffraction measurement performed *in-situ* during a tensile test for the 0.4 wt% C carbon steel with 8 vol% of cementite plates. The effect of lattice strain partitioning between phases was correctly predicted for the small deformation range of up to 3% of sample strain. However, the anisotropy effect was considered only for the ferrite phase.

Using X-ray diffraction, Che et al. (2007) demonstrated, that during mechanical loading and after unloading, the stress state in the ferrite and spheroidal cementite depends on the volume fraction and size of cementite particles. The role of the inter-lamellar spacing on the elastoplastic behaviour of C70 pearlitic steel has been investigated by Yahyaoui et al. (2014), using conventional X-ray diffraction during tensile tests coupled with the self-consistent model. It was established that the initial critical resolved shear stress (CRSS) of ferrite decreased with an increase of inter-lamellar spacing.

A micromechanical model based on the self-consistent scheme was developed by Taupin et al. (2013) in order to reproduce stress partitioning between phases in 0.4 wt% C steel containing 5.7 vol% of spheroidal cementite and to take into account the dislocation pile-up effect. The results were compared with stresses measured during an *in situ* tensile test using synchrotron X-ray diffraction. However, in the analysis of experimental data, only one reflection for each phase was considered, therefore the anisotropy of elastic and plastic deformation was not taken into account. It was found that to achieve a good estimation of the important difference between stresses in two phases, a third phase should be introduced. This so-called "third phase" represents finite intermediate layers in ferrite accounting for the accumulation of geometrically necessary dislocation (GND) at the ferrite-cementite interfaces. This assumption can be realistic with respect to the TEM studies of the deformed microstructure, discussed above. The developed model was inspired by that used in the modelling of elastic composites with spherical multi-coated inclusions as proposed by Cherkaoui et al. (1994) and Marcadon et al. (2007). In model calculations the ferrite is considered as an elastoplastic phase, which deforms and hardens through dislocation density evolution, the cementite is supposed to be purely elastic and the third phase layer together with cementite particle form a composite inclusion (Taupin et al., 2013). The thickness of this layer, assumed constant during plastic deformation, was calibrated in order to reproduce the elastic strain measurements and corresponding stress in ferrite and cementite. The estimated thickness of the hardened layer was 0.3 μm. The authors demonstrated that stress partitioning between cementite and ferrite was correctly predicted but only for sample strains higher than 5%. However, an important discrepancy between the model stress response and the experimental data was found for small deformations (lower than 5%), including elastic range of deformation and for Lüders plateau occurring in ferrite.

The finite element method (FEM) was also used to predict the elastoplastic deformation of composite material. This method was successfully applied by Young et al. (2007) in the case of spheroidal cementite inclusions. In this work, the load partitioning during elastic-plastic deformation has been investigated on the ultrahigh carbon steel (1.6 wt% C) with 34% of spheroidal Fe_3C particles, using synchrotron X-ray diffraction. It was shown that in the elastic range there is no load transfer between the microstructure constituents, due to the nearly equivalent elastic properties, since the macroscopic Young modulus is frequently considered equal to 210 GPa for α-Fe and 200 GPa for Fe_3C, whereas the average Poisson ratio is assumed around 0.29 for both phases (cf. Ledbetter, 2010; Nikolussi et al., 2008; Young et al., 2007). Young et al. (2007) showed that the load transfer occurred from the ductile ferrite to the

brittle Fe_3C spheroids during the plastic deformation of the steel and this effect was well predicted by FEM with the assumption of spherical inclusions. On the basis of measured α-Fe (220) and the Fe_3C (220) reflections the authors demonstrated that at sample strain equal to 0.7%, the effective stress (von Mises equivalent stress) localised in cementite was 2.3 times higher than the stress in ferrite and this ratio increased up to the value of 3.5 at 6.1% of sample strain. This result implies that load transfer from ferrite to cementite continues until the fracture of the steel.

The dual phase structure of pearlitic steels involves an inherent and a prospective elastic and plastic induced anisotropy, which could significantly affect the local and the overall material properties under various monotonic (Nikolussi et al., 2008; Young et al., 2007) and cyclic loading paths (Long et al., 2008) as a consequence of load transfer changes. Young et al. (2007) discussed the influence of anisotropy of elastic and plastic deformation in ferrite phase on a load transfer between grains. They showed differences in lattice strain evolution for measured *hkl* reflections and concluded that these evolutions are similar to those previously observed in the case of single phase ferritic steel. The elastic anisotropy of cementite was not seen in the elastic range of deformation, while the difference in lattice strain evolution was determined for different *hkl* reflections during the plastic deformation of pearlitic steel. In data analysis anisotropic X-ray elastic constants (XECs) based on Kröner model were used for ferrite, however isotropic elastic constants were based on macroscopic Young modulus and Poisson ratio.

Analysing lattice strains for different orientations of the scattering vector, a curvature of $sin^2\psi$ plots (for details see eg. Hauk, 1997) was observed by Young et al. (2007) during the plastic deformation of ferrite. This is evidence that significant second-order plastic incompatibility stresses, depending on the orientation of crystallite lattice, were generated in ferrite. The latter stresses usually arise in polycrystalline material because of the difference in the plastic behaviour of crystallites, leading to non-linearities of the $sin^2\psi$ plot, as observed by Wroński et al. (2007) in duplex steel and by Wawszczak et al. (2016) in ferritic and austenitic steels. On the other hand, linear character of $sin^2\psi$ plots measured by Young et al. (2007) for cementite, during whole deformation range, showed that this phase is deformed elastically. The problem of the second-order stresses in pearlitic steel is analysed in the present work.

Another model based on FEM calculations combined with EPSC model was developed by Oliver et al. (2004). In this case, the FE method was used for modelling of interphase stresses, while the intergranular interactions within ferrite phase were predicted by the EPSC model. The model results were compared with lattice strains measured by neutron diffraction during a tensile test in both phases of steel (1.0 wt% C) with 20% of spheroidal cementite. It was found that the partitioning of the lattice strains between phases as well as the difference between lattice strains for different *hkl* reflections were correctly predicted, however the anisotropy of cementite was not taken into account.

In above presented models of elastoplastic deformation, isotropic elastic constants were assumed for cementite phase. In many works the elastic behaviour of cementite was studied and different values of overall Young's modulus were reported ($E = 140–230$ GPa, cf. literature review given by Ledbetter (2010)). However, the *ab initio* calculations showed significant anisotropy of Fe_3C single crystals (Nikolussi et al., 2008), which was verified using synchrotron X-ray diffraction experiments (Nikolussi et al., 2008; Weisser et al., 2011). In the first work (Nikolussi et al., 2008) a massive Fe_3C layer, grown on the ferritic steel surface, was examined and an intermediate weighted model was used for the calculation of the X-ray elastic constants. The XEC were calculated as the weighted values between those obtained with Voigt (1928) and Reuss (1929) assumptions of homogenous stress or homogenous strain, respectively. It was shown that the measured values of XEC are well correlated with a mixture of 84% of Voigt and 16% of Reuss values, indicating an intermediate type of grain interaction, which is closer to the Voigt type one. The idea of an intermediate weighted model is developed in the present paper for the plastic range of deformation.

In the work of Weisser et al. (2011) the *ab initio* elastic constants were successfully verified using *in situ* synchrotron diffraction for bainitic 1% CrMoV steel under applied loads. The authors compared single crystal Young moduli in different crystallographic directions *hkl* (E_{hkl}) with the measured values. In general, a good agreement was found, however the effect of the polycrystalline matrix was not taken into account, which caused disagreement in the case of extreme E_{301} and E_{122} moduli.

In spite of the numerous experimental and modelling studies devoted to the understanding the micromechanical properties and phase interactions in pearlitic steels, a number of questions remain unsolved due to the complex microstructure and its evolution, phenomena occurring in ferrite lamella during plastic deformation and significant transfer of stresses between the phases. Therefore, in the present work, the micromechanical behaviour of fully pearlitic C70 steel with fine and coarse lamellar structure under tensile loading is studied using synchrotron X-ray diffraction method. The main goals of this work are to obtain the experimental characteristics of phase stress during elastoplastic deformation and, on the basis of these data, to determine the strengthening mechanisms occurring in fully lamellar pearlite. In addition, the elastic and plastic anisotropy and the related plastic incompatibility stresses are studied at the scale of individual phases and crystallites. To predict the elastoplastic behaviour of the studied steel, the idea of an intermediate model proposed previously by Nikolussi et al. (2008) for the elastic range of deformation is extended. The new method is based on the EPSC model developed by Lipinski and Berveiller (1989) and applied for two phase materials by Baczmański et al. (2016), Bonfoh et al. (2003), Hounkpati et al. (2016).

Table 1
Chemical composition of EN C70 pearlitic steel.

C	Si	Mn	S	P	Ni	Cr	Mo	Cu	Al	Fe
0.68	0.192	0.846	0.010	0.010	0.114	0.160	0.027	0.205	0.042	Balance

2. Experimental

2.1. Material

The pearlitic steel EN C70 (SAE 1070) investigated in this study was produced by the company ASCOMETAL France in the form of round bars with a diameter of 80 mm. The chemical composition of this steel is given in Table 1. Two annealing treatments reported in Table 2 were performed in order to obtain different microstructures in the same material. The resulting microstructure consists of entirely pearlite colonies having an average size of 7–8 μm with cementite lamellae (Fig. 1) arranged at different distances from each other (cf. Table 2), depending on the thermal treatment. In both materials, the volume fractions of the ferrite and cementite phases are 88 vol% and 12 vol%, respectively. More information related to the heat treatments and microstructure is provided in the previous works (Sidhom et al., 2015; Yahyaoui et al., 2014).

2.2. Measurements

The lattice strains were measured *in situ* during a tensile test for two samples of pearlitic steel (subjected to treatments HT1 and HT2, cf. Table 2) at the ID15 synchrotron beamline (ESRF, Grenoble, France). The applied high energy synchrotron radiation with wavelength $\lambda = 0.14256$Å and a beam size of 100 $\mu m \times$ 100 μm enabled transmission measurements in the interior of the samples having a square cross-section with a side length of 1.5 mm (Fig. 2 a). Two-dimensional diffraction patterns were recorded by a square CCD detector (Thales PIXIUM 4700) during time of expositions equal to 10 s with interval times of 5 s. The short time of data collection enabled to perform diffraction measurements *in situ* during a continuous tensile test. The example 2D diffraction image is presented in Fig. 2 b, where the visible rings correspond to different reflections coming from the ferrite phase. Due to a small volume fraction of cementite the intensity of diffraction pattern from this phase is relatively low and not seen in this figure. However, the experimental data recorded on the 2D detector with a high energy synchrotron beam allowed to analyse lattice strains also in cementite, which is not possible using a laboratory X-ray diffractometer. The diffractograms showing the diffraction peaks analysed in this work are presented in Fig. 3.

No significant changes in intensity along the diffraction rings were found, i.e. the crystallographic texture could be considered as negligible in both phases of the studied steel. The latter observation was confirmed by independent X-ray measurements of pole figures for ferrite phase using Cu K_α radiation on a laboratory diffractometer. Therefore, in the analysis of experimental data as well as in model calculations, a random distribution of crystallite orientations was assumed.

3. Methods of analysis

The data obtained from the ESRF experiments were processed with the Fit2D software (Hammersley et al., 2007), transforming the two-dimensional diffractograms into typical one-dimensional ones consisting of intensity dependence versus 2θ scattering angle. The one-dimensional diffractograms were obtained through the integration of 2D sectors with an angular size equal to $\Delta\psi = 15^\circ$ for cementite (because of low intensity of the recorded rings) and $\Delta\psi = 2^\circ$ for ferrite phase (Fig. 2 b). This procedure enables to analyse distortions of the circles correlated with lattice strains. The next step in data analysis is the use of the Multifit software (Merkel and Hilairet, 2015), which automatically fits the theoretical functions to the diffractograms, obtained by the Fit2D software. The positions of the diffraction peaks were found by adjusting the pseudo-Voigt function and the interplanar spacings $\langle d\rangle_{\{hkl\}}$ for *{hkl}* planes were determined from the Bragg law (the average values of $\langle d\rangle_{\{hkl\}}$ for symmetrically equivalent sectors shown in Fig. 2 b were computed). The procedure described above was applied for the initial samples, and then repeated for each load applied to the samples.

3.1. Lattice strains and phase stress determining

Two different types of analysis were performed for the diffraction data collected during the tensile test. In the first one, the relative lattice strains for the loaded sample with respect to the non-loaded material were calculated. This has been done for two orientations of the scattering vector, i.e. along x_3 - direction of applied load corresponding to the sector with centre at $\psi = 0^\circ$ and along x_2 – transverse direction corresponding to the sector with centre at $\psi = 90^\circ$ (cf. Fig. 2):

$$\langle \varepsilon_{33}\rangle_{\{hkl\}} = \frac{\langle d_{x3}\rangle^{\Sigma}_{\{hkl\}} - \langle d_{x3}\rangle^{0}_{\{hkl\}}}{\langle d_{x3}\rangle^{0}_{\{hkl\}}} \quad \text{and} \quad \langle \varepsilon_{22}\rangle_{\{hkl\}} = \frac{\langle d_{x2}\rangle^{\Sigma}_{\{hkl\}} - \langle d_{x2}\rangle^{0}_{\{hkl\}}}{\langle d_{x2}\rangle^{0}_{\{hkl\}}} \tag{2}$$

where: $\langle d\rangle^{\Sigma}_{\{hkl\}}$ and $\langle d\rangle^{0}_{\{hkl\}}$, respectively, are the interplanar spacings measured for a given applied stress Σ and for non-loaded sample

Table 2
Thermal treatments applied and characterization of EN C70 pearlitic steel (Yahyaoui et al., 2014).

Annealing heat treatment	Austenizing temperature (K)	Austenizing time (h)	Colling method	Inter-lamellar spacing (nm)	Colonies size (μm)	Grains size (μm)
HT1	1073	0.5	calm air	230	7.4	19
HT2	1323	0.11	blown air	170	7.9	26

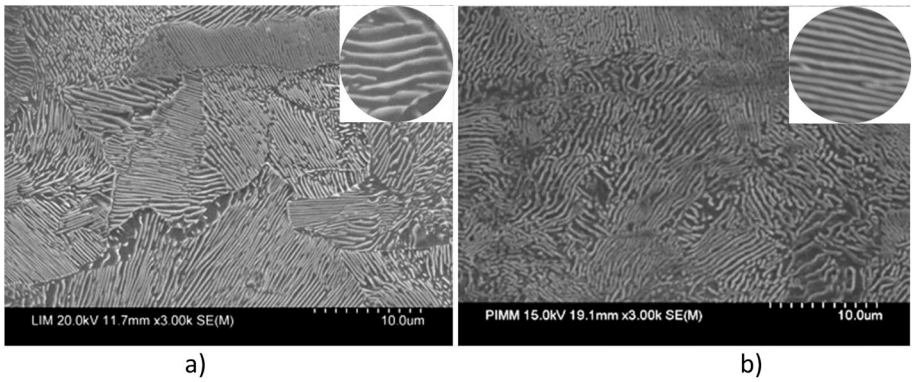

Fig. 1. Microstructures of C70 pearlitic steel after two types of heat treatment applied: (a) HT1 and (b) HT2 (cf. Table 2).

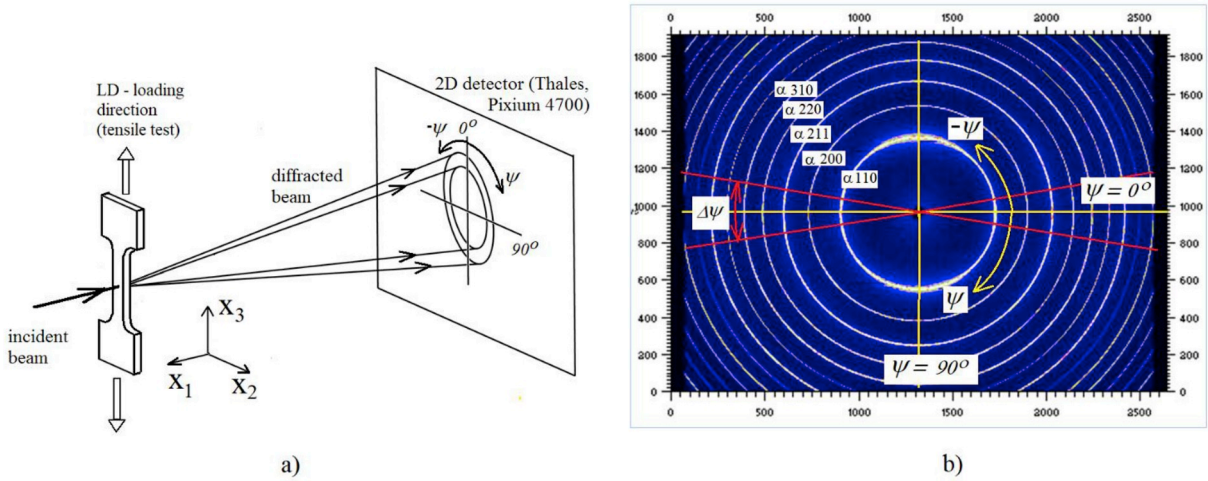

Fig. 2. The experimental setup used for lattice strain measurement at the ID15 synchrotron beamline (a) and the 2D image obtained for the studied pearlitic steel (b). The diffraction rings corresponding to reflections from ferrite (α phase) are indexed and two sectors with an angular size of $\Delta\psi$ are shown (the diffraction pattern corresponding to cementite is not visible due to relatively low intensity).

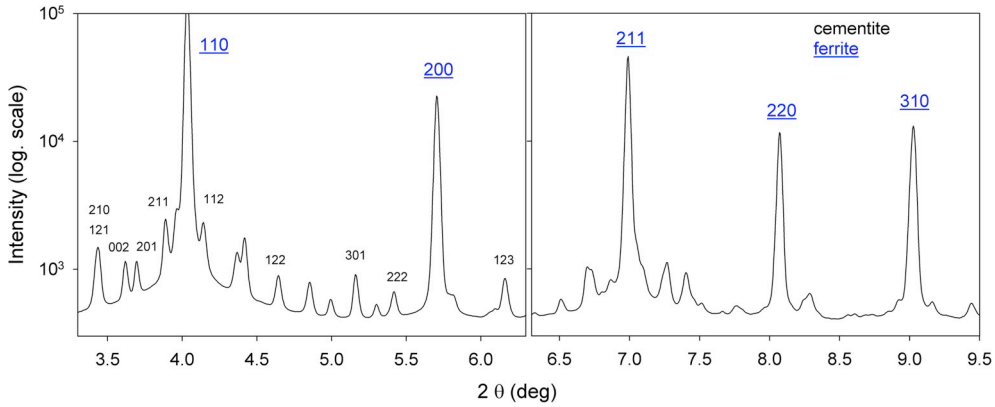

Fig. 3. Example diffractogram obtained for the studied pearlitic steel. The indices are shown for the peaks used in the analysis.

(initial, i.e. for $\Sigma = 0$), while the $< \ldots >_{\{hkl\}}$ brackets denote an average over the diffracting crystallites volume for a given reflection *hkl*. Indices x_3 or x_2 mean that the interplanar spacing was measured in the direction of the applied load or in the transverse direction, respectively.

In the next step of analysis the mean stresses in both phases were determined directly from diffraction data. To do this, the orientations of the scattering vector for different 2D sectors were defined by ψ angle, as shown in Fig. 2. Subsequently, parts of the intensity rings were integrated within the sectors and the interplanar spacings $< d_\psi >_{\{hkl\}}$ were calculated for the reflections provided in Table 3. The method of stress analysis based on the measured $< d_\psi >_{\{hkl\}}$ spacings is shortly presented in Appendix A. At first, using the measurements obtained for the initial non-deformed sample and assuming negligible hydrostatic stresses (Young et al., 2007), the stress free lattice parameters were determined for cementite and ferrite using the Rietveld method (Table 3). It was also found that the deviatoric stresses in both phases of the initial sample are close to zero, comparing to the range of uncertainty (Appendix A). Then the lattice parameters $< a_\psi >_{\{hkl\}}$ were determined for the samples subjected to different loads and the three principal components of stress tensor were found for each load, assuming the stress free parameters given in Table 3 and axial symmetry of the sample. In the calculations, the second-order incompatibility stresses were also taken into account (for details see Appendix A). The example dependences of lattice parameters $< a >_{\{hkl\}}$ vs. $sin^2\psi$ in each phase, measured and recalculated for the initial and loaded sample, are shown in Figs. A1 and A2.

3.2. Model calculations

The interpretation of the results was done with the help of a model in which different types of stress localisation in the phases were considered. Due to a large aspect ratio of the cementite lamellae and extremely complex microstructure of cementite the interpretation of experimental results with elastoplastic models is quite problematic. Therefore, in this work the interaction between cementite and ferrite, described by the Eshelby type models (Eshelby, 2007), was modified.

The self-consistent calculations using EPSC model (Baczmański et al., 2016; Baczmański and Braham, 2004; Lipinski and Berveiller, 1989) were performed for 10,000 inclusions, representing ferrite (88 vol%) and cementite (12 vol%). As the texture of the examined material was insignificant, the random initial orientations of the lattice were generated for pearlite grains in both phases. At first, the model calculations with spherical cementite inclusions were performed (it was treated as the reference result) and next, the shape of the inclusions was modified to mimic the shape of cementite lamella. Different orientations of the habit plane with respect to the cementite lattice (Das, 2018; Kante and Leineweber, 2019; Zhang et al., 2007; Zhou and Shiflet, 1992) were also tested. The model predicted lattice strains and macromechanical stress-strain plots were compared with experimental data obtained for purely elastic range of deformation. It was found that the best agreement between experiment and model was obtained for plate shape of cementite and ferrite lamellae with the axes ratios $a'/b' = 1$ and $a'/c' = 2.5$, randomly orientated with respect to the sample. The assumed habit plane was $(010)_c$ in cementite and $(11\overline{2})_f$ in ferrite, as given by Bagaryatsky crystallographic orientation relationships (Das, 2018; Kante and Leineweber, 2019; Zhou and Shiflet, 1992). The flat ellipsoidal inclusions with a habit plane parallel to the interphase boundary were used in calculations performed for the elastic and plastic range of deformation. However, it should be emphasised that the results obtained for Bagaryatsky orientation relationships are not significantly different compared to those obtained assuming Isaichev or Pitch-Petch relationships and corresponding habit planes (Kante and Leineweber, 2019; Zhou and Shiflet, 1992). Slightly worse agreement between experiment and model prediction was found in the case of spherical inclusions having random orientations of habit planes.

The plastic deformation of ferrite was described by the slip systems: <111> {211} and <111> {110}, having initially the same value of CRSS. It was assumed that cementite lamella do not undergo plastic deformation. The elastic properties of the cementite and ferrite crystallites were described by the elastic constants given in Table 4. During plastic deformation, the critical resolved shear stresses, stresses localised in crystallites and lattice orientations were varied according to algorithms described by Lipinski and Berveiller (1989), Baczmański and Braham (2004), Baczmański et al. (2016).

In model calculation initial stress was assumed to be equal zero for all inclusions belonging to cementite and ferrite phases (this assumption is based on the stress measurement performed for the initial sample, presented in Appendix A).

Assuming that only the ferrite phase undergoes plastic deformation, the hardening of the ferrite was described by the phenomenological Voce law. This law describes the evolution of CRSS during plastic deformation in a given crystallite g within ferrite phase according to the equation (Neil et al., 2010; Tome et al., 1984):

$$\tau_{Voce}^{g,fer} = \tau_0^{fer} + \left(\tau_1^{fer} + \theta_1^{fer}\vartheta^{g,\,fer}\right)\left[1 - exp\left(-\frac{\theta_0^{fer}}{\tau_1^{fer}}\vartheta^{g,\,fer}\right)\right] \tag{3}$$

where:

Table 3
Lattice parameters determined from the initial HT2 sample and the reflections available for different analyses.

Phase	Lattice parameters -stress free values (Å)	Reflection used in stress analysis and to calculate mean lattice strains in phases	Reflections available during elastic deformation
Cementite (orthorhombic)	$a_0 = 5.0689\ (4), b_0 = 6.7493\ (7), c_0 = 4.5116\ (5)$	121/210,122,123,222,301	002,201,211,112, 121,122,123,222,301
Ferrite (bcc)	$a_0 = 2.86364(2)$	110, 200, 211, 220, 310	110, 200, 211, 220, 310

Table 4
Single-crystal elastic constants of cementite (Nikolussi et al., 2008) and ferrite (Simmons and Wang, 1971) used in data analysis and modelling. In the case of cementite the elastic constants were obtained using the ab-initio method.

[GPa]	C_{11}	C_{22}	C_{33}	C_{44}	C_{55}	C_{66}	C_{12}	C_{13}	C_{23}
Cementite	385	341	316	13	131	131	157	162	167
Ferrite	231	–	–	116	–	–	134	–	–

τ_0^{fer} - initial critical shear stress necessary to start crystallographical glide in ferrite,
τ_1^{fer} - the shear stress back-extrapolated from the terminal linear hardening region,
θ_0^{fer}, θ_1^{fer} - are the initial and final slopes of the hardening curve in ferrite, respectively and $\vartheta^{g,\,fer} = \sum_t \gamma^t$ is a sum of total shear strains γ^t for all slip systems t activated in crystallite g.

The idea of using empirical law for the plastic behaviour of the ferrite phase directly comes from Eq. (1), which correctly describes the yield stress evolution for fully pearlitic steel having lamellar structure, as shown by Bouaziz and Le Corre (2003) and Allain and Bouaziz (2008). In this work, a similar Eq. (3) is assumed to describe the plastic behaviour of ferrite within lamellar pearlite. The latter equation is written for critical shear stress $\tau_{Voce}^{g,fer}$ necessary to start crystallographic slip in ferrite crystallite g. This means that Eq. (3) is defined for a smaller scale than Eq. (1). As discussed in the Introduction, the initial yield of pearlite (friction stress σ_f^{per} and size strengthening $\frac{\mu Mb}{s}$ in Eq. (1)) depends on the initial hardness of ferrite, and it is represented by the initial critical shear stress τ_0^{fer} in Eq. (3). The third term of Eq. (1) describing pearlite hardening depends only on the strain of pearlite, while in the corresponding second term of Eq. (3) takes into account the hardening of the ferrite depending on total shear strain $\vartheta^{g,fer}$ in given plastically deformed crystallite g (i.e., hardening is considered at smaller scale in Eq. (3) comparing to Eq. (1)).

In principle, the EPSC model was used to calculate the interaction between crystallites and consequently stress partitioning between phases. However, it found that the interaction of the Eshelby inclusion with elastoplastic self-consistent matrix is not sufficient to correctly reproduce the experimental results. To overcome the above problem, a similar approach as proposed for elasticity by Nikolussi et al. (2008) was extended to plastic deformation. We decided to modify the strain concentration tensor A_{ijkl}^{sc} predicted by the self-consistent model, which relates macroscopic $\dot{E}_{kl}$ and local $\dot{\varepsilon}_{ij}$ total strain rates (elastic plus plastic) or analogical stress concentration tensor B_{ijkl}^{sc} relating macroscopic $\dot{\Sigma}_{kl}$ and local $\dot{\sigma}_{ij}$ stress rates (dot means time derivative):

$$\dot{\varepsilon}_{ij} = A_{ijkl}^{sc}\dot{E}_{kl} \quad \text{and} \quad \dot{\sigma}_{ij} = B_{ijkl}^{sc}\dot{\Sigma}_{kl} \tag{4}$$

The modified strain concentration tensor $\boldsymbol{A}$ can be constructed as the weighted mean of the self-consistent tensor $\boldsymbol{A}^{sc}$ and identity four rank tensor $\boldsymbol{I}$ being a strain concentration tensor in the case of homogenous total strain assumption ($\dot{\varepsilon}_{ij} = \dot{E}_{ij}$), as in simplified Lin model (Lin, 1957, 1971):

$$\boldsymbol{A} = \eta\,(\boldsymbol{A}^{sc} - \boldsymbol{I}) + \boldsymbol{I} = \eta\boldsymbol{A}^{sc} + (1-\eta)\,\boldsymbol{I} \quad \text{for} \quad \eta \in [0,1] \tag{5}$$

where scalar factor η represents the contribution of the self-consistent tensor $\boldsymbol{A}^{sc}$.

Similarly, the modified strain concentration tensor $\boldsymbol{B}$ can be expressed as the weighted mean of the self-consistent tensor $\boldsymbol{B}^{sc}$ and identity four rank tensor $\boldsymbol{I}$ corresponding to homogenous stress distribution ($\dot{\sigma}_{ij} = \dot{\Sigma}_{kl}$), as in simplified Sachs model (Sachs, 1928):

$$\boldsymbol{B} = \xi\,(\boldsymbol{B}^{sc} - \boldsymbol{I}) + \boldsymbol{I} = \xi\boldsymbol{B}^{sc} + \,(1-\xi)\,\boldsymbol{I} \quad \text{for} \quad \xi \in [0,1] \tag{6}$$

where scalar factor ξ represents the contribution of the self-consistent tensor $\boldsymbol{B}^{sc}$.

The physical meaning of the above defined localisation tensors and their derivation based on the Lipinski-Berveiller model are given in Appendix B. In this Appendix also the equivalent formulation of Eqs. (5) and (6) for the Hill model (Hill, 1965) is presented (cf. the definition of weighting parameter $\alpha_H \in [0,\infty)$ in Eq. (B16)). Moreover, it was shown that if the value of η coefficient in Eq. (5) is equal to 1 (or $\alpha_H = 1$) the pure self-consistent model is assumed, if $\eta < 1$ (or $\alpha_H > 1$) the model shifts partially to the Lin's assumption, which is obtained for $\eta = 0$ (or $\alpha_H \to \infty$). Analogically, ξ in Eq. (6) is equal to 1 for the pure self-consistent model, $\xi < 1$ (or $\alpha_H < 1$) assumption shifts stress localisation towards the Sachs type model, obtained for $\xi = 0$ (or $\alpha_H = 0$). It can concluded that ξ and η inform us how far the real interaction between crystallites or phases is from this predicted by EPSC model.

It should be emphasised that the above introduced elastic-plastic mixed (EPM) model based on Eqs. (5) and (6) (or Eq. (B16)) is similar to this proposed by Berveiller and Zaoui (1978) in which the α plastic accommodation parameter (Eq. (B17)) was used to modify the interaction of a given grain with the surrounding matrix (for details see Appendix B). In turn, the Berveiller and Zaoui model is approaching the elastic type Kröner model (Kröner, 1961) for $\alpha = 1$ and upper Lin's boundary for $\alpha = 2$. The accommodation parameter α take into account both the "plastic softening" of the matrix and other physical effects not connected with this phenomenon.

When the Berveiller-Zaoui model is fitted to experimental data, the value of classical plastic accommodation parameter α informs us how far the results are from the elastic Kröner model (α is usually in the range 0.01–0.1). On the other hand the η and ξ (or α_H) determine deviation from the incremental Lipinski-Berveiller (or Hill) model, in which the "plastic softening" of the matrix is already

taken into account and grains interaction depends on the tangent modulus tensor $\boldsymbol{L}_{sc}$ (or constrain tensor $\boldsymbol{L}_{sc}^{*}$ in Eq. (B16)), which changes during deformation. Because the difference between the Kröner model and the incremental Hill (or Lipinski-Berveiller) model varies with deformation (Hutchinson, 1970), there is no straightforward relation between the parameter α and the parameters introduced in this work, i.e. η and ξ (or α_H). The approximate relations between all parameters are visualised in Fig. 4, where additionally the bound of Taylor (1938) is also shown. However, the latter bound cannot be compared with Hill or Lipinski-Berveiller model due to Taylor's unrealistic assumption of homogenous plastic strain (not total strain), which leads to a rigid matrix excluding the elastic interaction. It should be underlined that the upper bound of the EPM model is the Lin's assumption of homogenous total strain, when the plastic strain of inclusion is fully compensated by the elastic deformation of the matrix.

The undertaken EPM approach enables to consider the interactions between phases, which can be estimated on the basis of experimental results. The fraction of Lin/Sachs model can be adjusted so the partitioning of the stresses between phases can be tuned. For example a bigger contribution of the Lin model ($\eta < 1$) in the plastic range of deformation causes that the cementite phase carries a higher stress than predicted by the self-consistent model.

In this work, Eq. (5) was used, because only the shift of the strain localisation tensor towards the assumption of homogenous strain (Lin model) was observed. As presented in the next section, it was found that the self-consistent model correctly predicted partitioning of the stresses between phases during elastic deformation, however definitely to low stress is localised in the cementite phase at the beginning of plastic deformation. This means that the contribution of the Lin model (given by the value of $1-\eta$) must be significantly increased just above the yield point. Subsequently, the stress localisation again approaches to this predicted by self-consistent model, i.e. the value of $1-\eta$ must decrease. Therefore, the Lin model contribution can be described by the asymmetrical peak-shaped relationship of $(1-\eta)$ vs. the sample strain E during plastic deformation (cf. Fig. 6 a in section 4.1). In such a case, the η parameter being a quantitative measure of the self-consistent model contribution, can be approximated by a phenomenological function, which allowed to adjust the model calculations to experimental data (cf. Fig. 6 a):

$$\eta = 1 - A\, exp\left[-\frac{1}{B}\left\{ ln\left(\frac{E}{C}\right)\right\}^{2}\right] \tag{7}$$

where A,B,C are the adjusted parameters without physical interpretation and $E = E_{33}$ is the sample strain in the direction of the applied load (cf. Fig. 2 b).

3.3. Stress localisation in the phases

It is essential to describe quantitatively the stress partitioning between phases. This was previously done on the basis of phase total stresses and strains determined in the direction of the applied load (Bouaziz and Buessler, 2004). In the present work a more precise description of stress partitioning, based on the stress localisation tensor $\boldsymbol{B}^{sc}$, is used. The advantage of this method is that the components of the $\boldsymbol{B}^{sc}$ tensor can be determined from the experimental diffraction data and the stress localisation both in tensile and in the transvers directions are taken into account. This method was already proposed by Baczmański et al. (2012) for duplex steel and the components of localisation tensor were successfully compared with the self-consistent model. The aim of the present work is to determine localisation tensors for both phases of pearlitic steel directly from experimental data and to verify the localisation tensor calculated from the model used.

The classical stress rate localisation tensor B_{ijkl}^{ph} relates the rate of stress in a given phase with the rate of applied macrostresses and can be defined by the formula:

$$\dot{\sigma}_{ij}^{ph} = B_{ijkl}^{ph}\,\dot{\Sigma}_{kl} \tag{8}$$

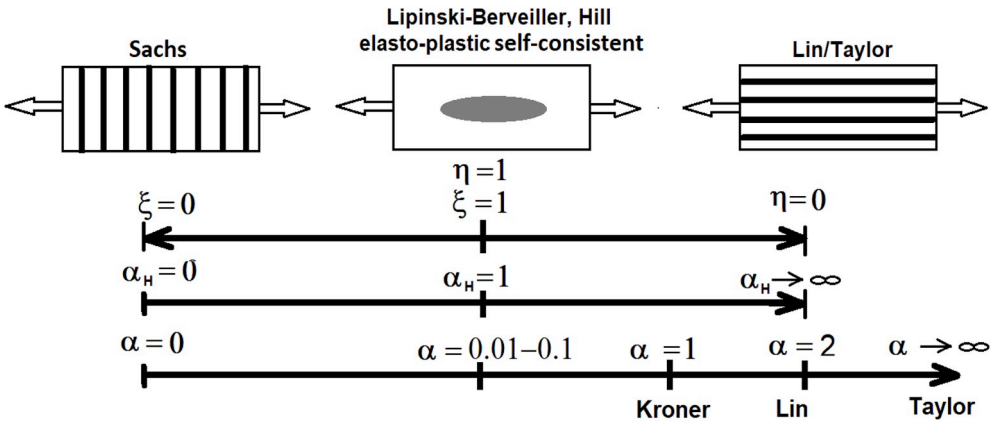

Fig. 4. Relations between η, ξ, α_H and α parameters defined for different types of elastoplastic.

where $\dot{\sigma}_{ij}^{ph}$ and $\dot{\Sigma}_{kl}$ are respectively the mean stress rates for the phase *ph* and the rate of applied stresses.

For small increments, it can be written:

$$\Delta\sigma_{ij}^{ph} = B_{ijkl}^{ph}\,\Delta\Sigma_{kl}. \tag{9}$$

In the case of tensile test and quasi-isotropic sample, the axial symmetry is assumed, therefore the main components of the stress localisation tensor can be determined from experiment and model results if the appropriate increments of the stresses are known, i.e.:

$$B_{3333}^{ph} = \Delta\sigma_{33}^{ph}/\,\Delta\Sigma_{33} \quad \text{and} \quad B_{1133}^{ph} = B_{2233}^{ph} = \Delta\sigma_{11}^{ph}/\,\Delta\Sigma_{33} = \Delta\sigma_{22}^{ph}/\,\Delta\Sigma_{33} \tag{10}$$

where the x_3 axes is defined along the applied load, i.e. $\Sigma_{33} = \Sigma$.

4. Analysis and discussion of the results

The analysis of the synchrotron data was performed in three steps. At first, the weighted EPM model proposed above was tested for both elastic and plastic deformation ranges by comparing model prediction with the macromechanical behaviour and the lattice strains measured in two perpendicular directions during a tensile test. As the results, the optimal model parameters (τ_0^{fer}, τ_1^{fer}, θ_0^{fer} and θ_1^{fer} in Eq. (3), and η or ξ in Eq. (5) or (6)) for the best agreement between theoretical and experimental data were found. What is more the elastic constants of ferrite and cementite, as well as anisotropy of elastoplastic deformation were verified analysing the lattice strains measured for different reflections *hkl*. Subsequently, the partitioning of the stresses between phases was studied and discussed. To do this, the mean phases stresses were calculated from the measured lattice strains, including von Mises and hydrostatic stresses. Finally, the partitioning of the stresses was qualitatively discussed on the basis of the determined components of the stress localisation tensor. In each step of the analysis the comparison between experimental and model results was checked.

The obtained experimental and model result allow us to discuss the dominating reasons for pearlite strain strengthening and to confront the conclusions drawn with previously published papers.

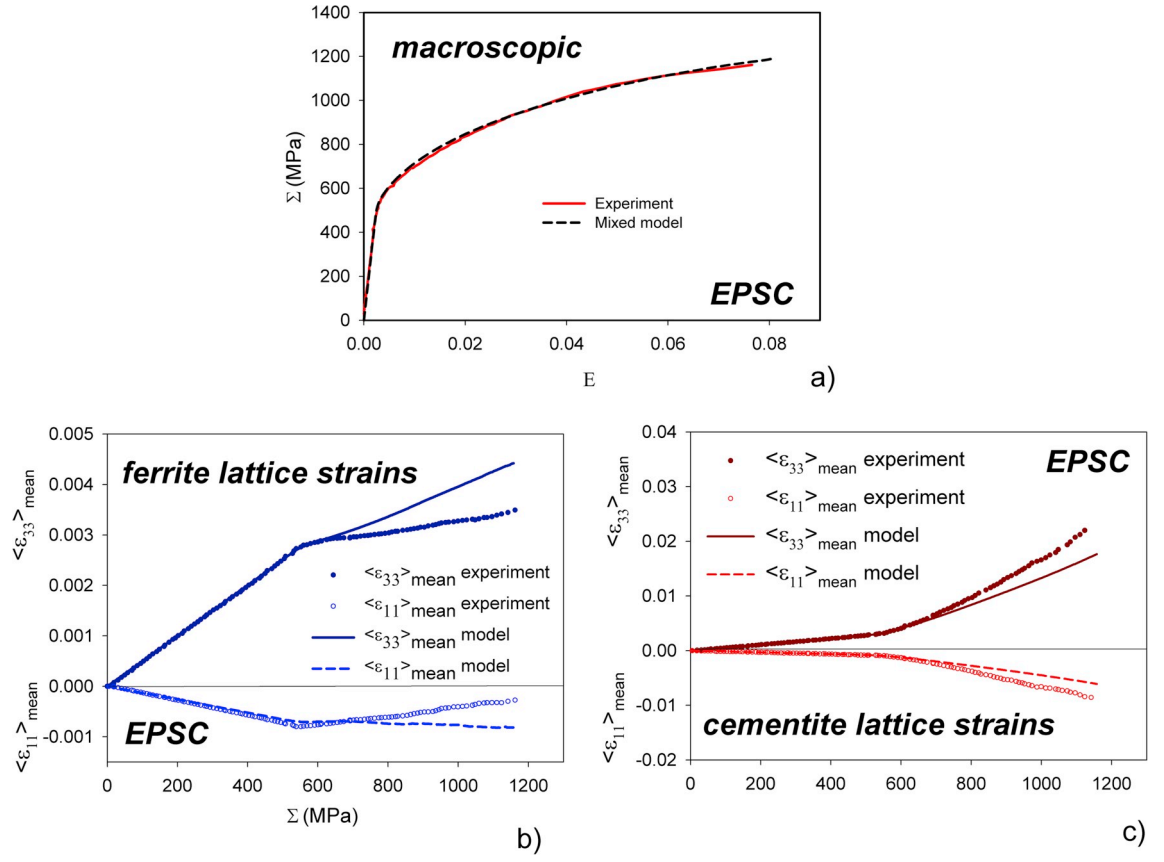

Fig. 5. Experimental stress-strain curve (a) and arithmetic mean of lattice strains (for reflections given in Table 3) in both phases of the specimen HT2 (b,c) are compared with EPSC model predictions, assuming spherical inclusions of cementite. The mean lattice strains in the direction of the applied load ($<\varepsilon_{33}>_{mean}$) and in the transverse direction ($<\varepsilon_{22}>_{mean}$) are shown as a function of the applied macrostress.

4.1. Tuning of the model based on strain evolution

The first adjustment of the model to experimental data was performed for the unmodified EPSC model assuming $\eta = \xi = 1$ in Eq. (5) or (6). It was found that a good agreement for the macroscopic data (Fig. 5 a) was obtained for unreasonable values of Voce law parameters for ferrite phase ($\tau_0^{fer} = 230$ MPa, $\tau_1^{fer} = 120$ MPa, $\theta_0^{fer} = 1200$ MPa, $\theta_1^{fer} = 10$ MPa), i.e. the predicted work hardening for ferrite phase seems to be too strong. Indeed, the diffraction experiment has shown that lattice strains in phases (cf. Eq. (2)) are not correctly predicted by the model during plastic deformation. As presented in Fig. 5, the arithmetic mean values of lattice strains measured for sets of reflection in each phase (specified in Table 3) do not agree with the corresponding model values in the plastic range of deformation. It can be concluded that in theoretical calculations the work hardening is definitely too strong for the ferrite phase, while the stress localised in cementite is too low.

Tuning of the model parameters was done in order to fit the predicted evolution of mean lattice strains in both phases as well as macroscopic stress vs. strain plot to the experimental results (Fig. 6 c). It was found that the agreement between model and experiment can be obtained only when the strain localisation tensor is expressed by Eq. (5) and the parameter η is adjusted. The optimal parameters describing the hardening process (according to Voce law, Eq. (3)) as well as for the evolution of η interaction parameter (Eq. (7)) are given in Table 5, for two studied samples. Additionally, the variation of η with sample strain $E = E_{33}$ is presented Fig. 6 a, and compared with the mechanical Σ vs. E curve shown in Fig. 6 b. It was found that in order to obtain a good fit of the micromechanical tensile plot as well as the evolution of lattice strains, the model should be shifted from self-consistent toward Lin model (Lin, 1957) in the early stages of plasticity and then back toward self-consistent at higher strains.

Different values of critical resolved shear stress (τ_0^{fer}) were determined for ferrite phase in HT1 and HT2 specimens, while the same parameter θ_1^{fer} was used to characterise a linear, isotropic and very small hardening of ferrite in both samples (assuming $\theta_0^{fer} = \theta_1^{fer}$ and $\tau_1^{fer} \to 0$), which was observed in the experimental plot in Fig. 6 b. The simulation result with the parameters given in Table 5 shows a very good agreement between the model and the measurements for the predicted mechanical curves (Fig. 6 b) as well as for the mean lattice strains in each phase (Fig. 6 c and d). Some disagreement occurred for lattice strains for relatively large deformation of HT1 specimen.

It should be emphasised that the value of η parameter results in modification of the effective strain concertation tensor $\boldsymbol{A}$ (cf. Eq. (5)) and consequently stress partitioning between phases. The same evolution of η as a function of sample stain E is observed for both studied samples HT1 and HT2 (cf. Fig. 6 a and Table 5). In both samples, the elastic range is well predicted by pure self-consistent model ($\eta = 1$), but at the beginning of plastic deformation of ferrite a strong interaction between phases is observed (model shifts toward to Lin's approach, i.e. $\eta \approx 0.8$). Next, the evolution of microstructure leads again to a weakening of interaction, which can be related to changes in distribution and/or cracking of cementite lamellae (η is closer to 1).

The evolutions of lattice strains are perfectly predicted for the whole range of deformation in the case of sample HT2, while for sample HT1 some lattice strain relaxation (not predicted by the model) is seen at the end of the tensile test. The mean experimental lattice strains seem to tend to higher absolute values for ferrite phase while those measured for cementite go to lower absolute values. This effect can be caused by the inversion of stress partitioning due to the damaged cementite lamellae. Indeed, fragmentation of the lamellae was observed in the HT1 sample after tensile tests (Yahyaoui et al., 2014).

In the next step of the analysis, the anisotropy of elastic and plastic behaviour of the phases is discussed. To do this the lattice strains ($< \varepsilon_{33} >_{hkl}$) evolution for individual *hkl* reflections are compared with the model prediction. The results of tensile test in the elastic range of deformation for the specimen HT2 are presented in Fig. 7 a, where experimental results are compared with the EPM model for both phases and for all *hkl* reflections separately. The calculations in the elastic range of deformation were performed for $\eta = 1$, which leads to a pure EPSC model. It can be concluded that the self-consistent model with the assumption of plate inclusions of cementite perfectly predicts the anisotropy of elastic strains in ferrite and cementite. To analyse the anisotropy of elastic properties in both phases the values of so-called diffraction Young modulus E_{hkl} are calculated from the linear part of lattice strains $< \varepsilon_{33} >_{\{hkl\}}$ vs. applied stress Σ dependence, i.e.:

$$E_{hkl} = \frac{\Sigma}{< \varepsilon_{33} >_{\{hkl\}}} \tag{11}$$

The graphs in Fig. 7 b show the correlation between measured and calculated Young modulus for groups of crystallites corresponding to different *hkl* reflections. A very important conclusion from these graphs is that the Young modulus (E_{hkl}) is quite similar for both phases, i.e. the E_{hkl} values are in the range of $180 - 240$ *GPa* for ferrite and $160 - 260$*GPa* for cementite. Moreover, the predicted overall Young modulus for pearlite is $E_{hkl} = 220$ *GPa*, hence the average properties of the matrix considered in the model calculations are isotropic (no texture) and almost equal for both phases as well as for the overall material. This is probably the reason for the good

Table 5
Parameters describing hardening of ferrite and evolution of weighting parameter η in EPM model.

Specimen	Hardening parameters for ferrite (Eq. (3)), assuming $\theta_0^{fer} = \theta_1^{fer}$ and $\tau_1^{fer} \to 0$		Constants determining evolution of η parameter (Eq. (7))		
	τ_0^{fer} (MPa)	θ_1^{fer} (MPa)	A	B	C
HT1	145	50	0.19	0.8	0.0138
HT2	230	50			

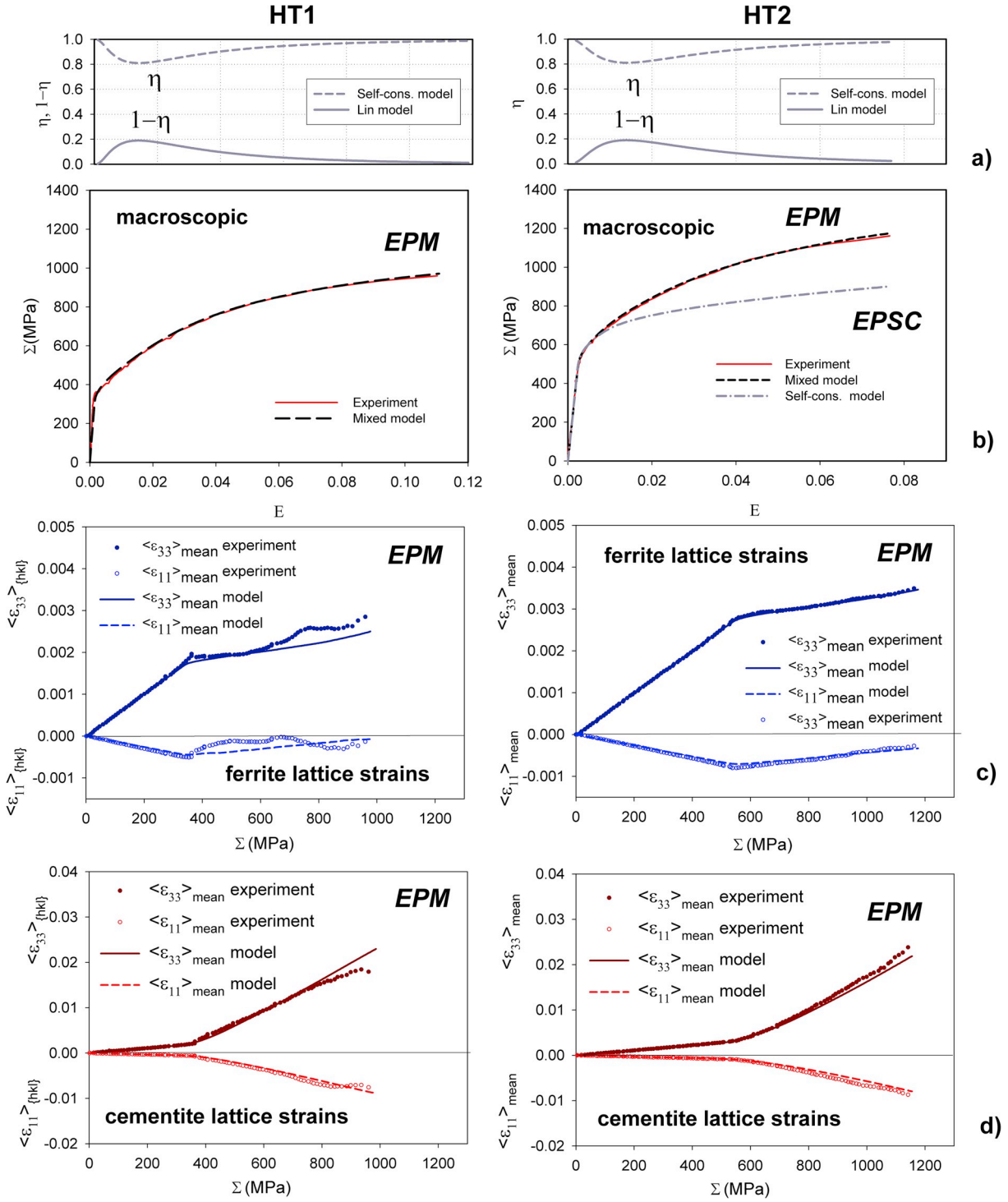

Fig. 6. Evolution of interaction parameter η (a) compared with experimental mechanical stress-strain curves (b), and arithmetic mean of lattice strains (c and d) for the reflections given in Table 3 in both phases of specimens HT1 (left) and HT2 (right). Mechanical stress-strain plot and lattice strains are compared with EPM model predictions (a–d), assuming the weighted method with the parameters given in Table 5 (in figure b also the macromechanical curve simulated by pure EPSC model is shown).

prediction of stress localisation by the EPSC model (within the elastic range of deformation) with the simplified assumption of plate shape of cementite inclusions, in spite of real complex lamellar structure of this phase. The presented results confirm the hypothesis of the elastic anisotropy measured using different reflections, which is well predicted for both phases. In the case of ferrite the

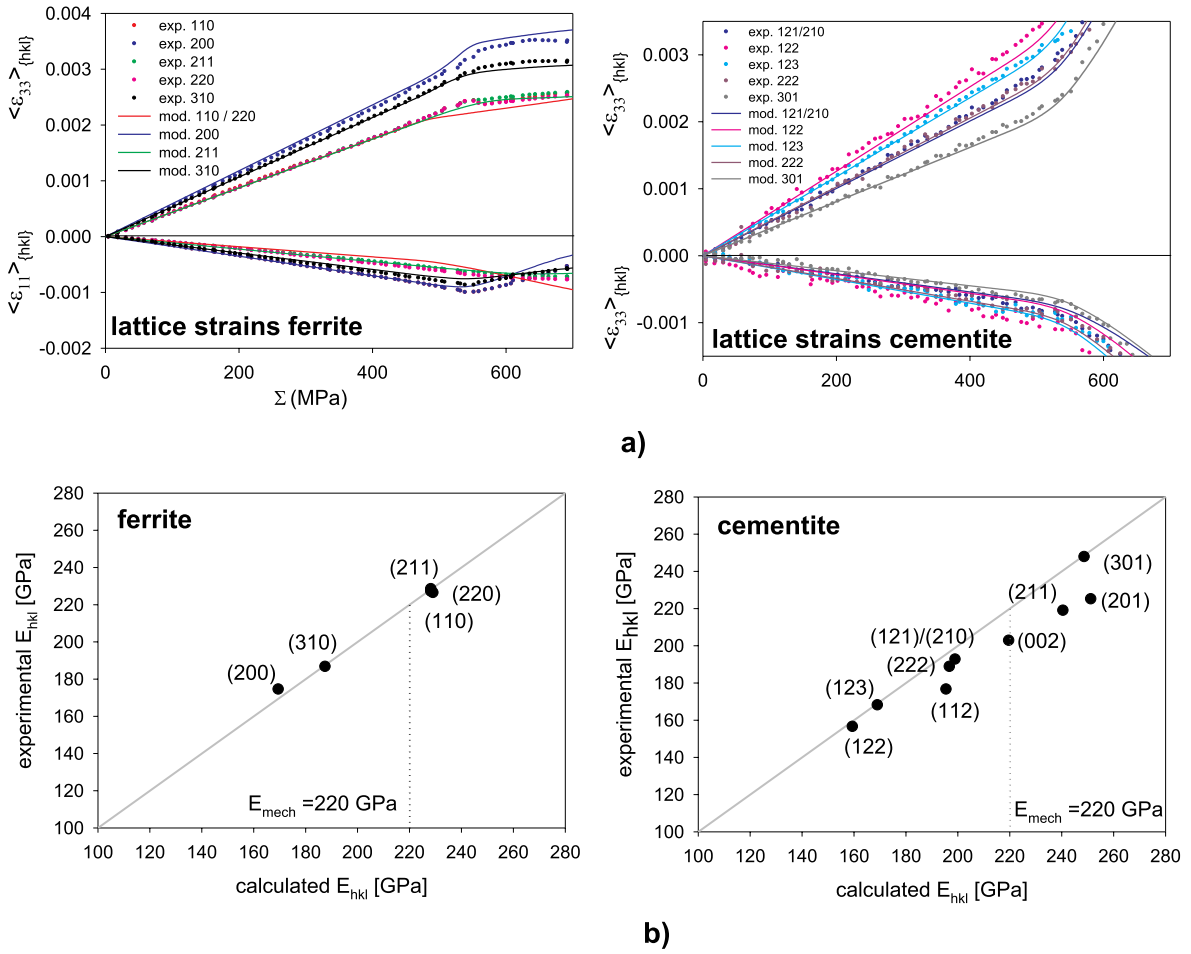

Fig. 7. Lattice strains $< \varepsilon_{33} >_{hkl}$ and $< \varepsilon_{11} >_{hkl}$ measured within the elastic range of deformation for the individual reflections *hkl* in both phases of the specimen HT2, compared with pure EPSC model (a) and correlation of the experimental diffraction Young moduli with model predicted values (b).

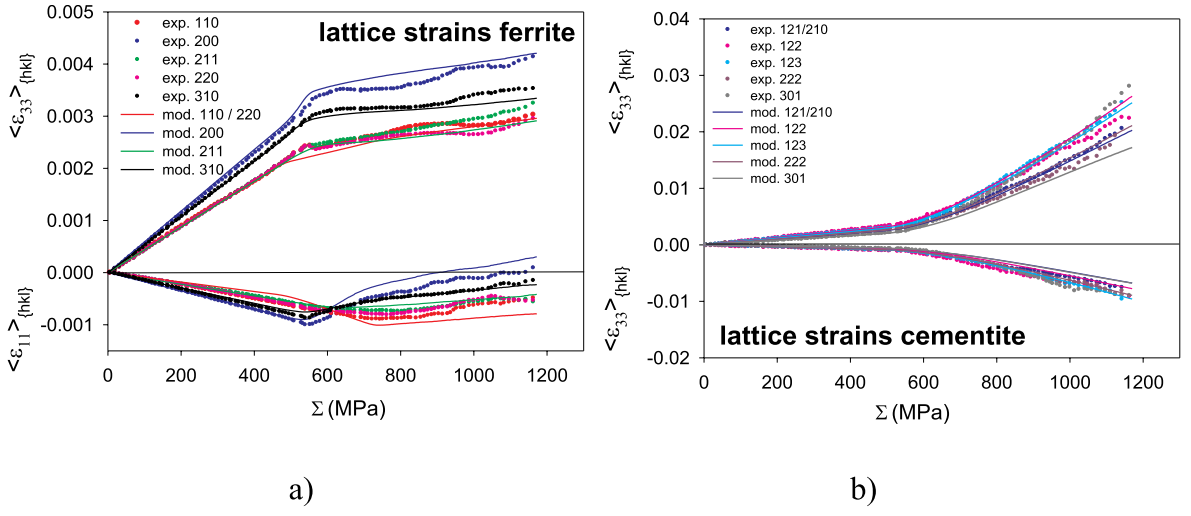

Fig. 8. Measured lattice strains $< \varepsilon_{33} >_{hkl}$ and $< \varepsilon_{11} >_{hkl}$ for the individual reflections *hkl* in ferrite (a) and cementite (b) compared with the weighted EPM model for the whole deformation range (specimen HT2). The simulation was performed with the parameters given in Table 5.

experimental results correlate perfectly with the model prediction, while for cementite the values of E_{hkl} are more scattered and slightly deviate from the correlation line (Fig. 7 b). The latter disagreement can be caused by the systematic inaccuracy of the single-crystal elastic constant used in the self-consistent prediction (the *ab initio* SEC were applied for cementite, Table 4), by the above mentioned problem of the proper calculation of stress/strain localisation for lamellar shape of inclusions or/and by experimental uncertainties of the diffraction peak positions due to low intensities of cementite reflections.

In Fig. 8 the behaviour of lattice strains $< \varepsilon_{33} >_{hkl}$ and $< \varepsilon_{11} >_{hkl}$ during a full range of elastoplastic deformation is compared with the model prediction. It can be concluded that during plastic deformation of ferrite the variation of lattice strains measured using different *hkl* reflections and the effect of lattice strain anisotropy is correctly predicted for ferrite in both measured directions. However, in the case of cementite the anisotropy is not correctly simulated, i.e. the resulting predicted lines do not correspond to experimental points, and only the range of anisotropy is well reproduced. The latter disagreement is probably caused by the complex shape of cementite lamellae and the fact that the introduced η parameter improved calculation of the mean stress/strain localisation in the cementite phase but the use of a single weighting parameter is not enough to correctly predict the interactions of cementite lamella.

Also interesting is the wavy-character of the lattice strains vs. applied stress dependences observed in the plastic range of deformation for ferrite in sample HT2 (Fig. 8 a). Such fluctuations are not seen in the case of cementite because, even if they exist, they are not significant comparing to the large strain increase in this phase (compare strain scales for both phases in Fig. 8). Surprisingly, the fluctuations in ferrite disappear when the mean strain is calculated for all *hkl* reflection measured in HT2 sample (cf. Figs. 8 a and Fig. 6 c, on the right). This means that the strains fluctuations depend on the statistics of the pearlite grains contributing to the selected reflections *hkl* (see large pearlite grain size in Table 2) and reflect the transfer of stresses between these grains or other stress heterogeneities at a larger scale than pearlite grain size (cf. Nakada et al., 2009). These stress heterogeneities oscillate during plastic deformation as seen in Fig. 8 a and they are not taken into account in the model calculations. When a large number of grains contribute to the mean lattice strain calculated for all *hkl* reflections, the fluctuations disappear (Fig. 6 c, on the right) because the local heterogeneities are averaged to zero. It can be also seen that in the case of sample H1 the fluctuations are seen even for the mean lattice

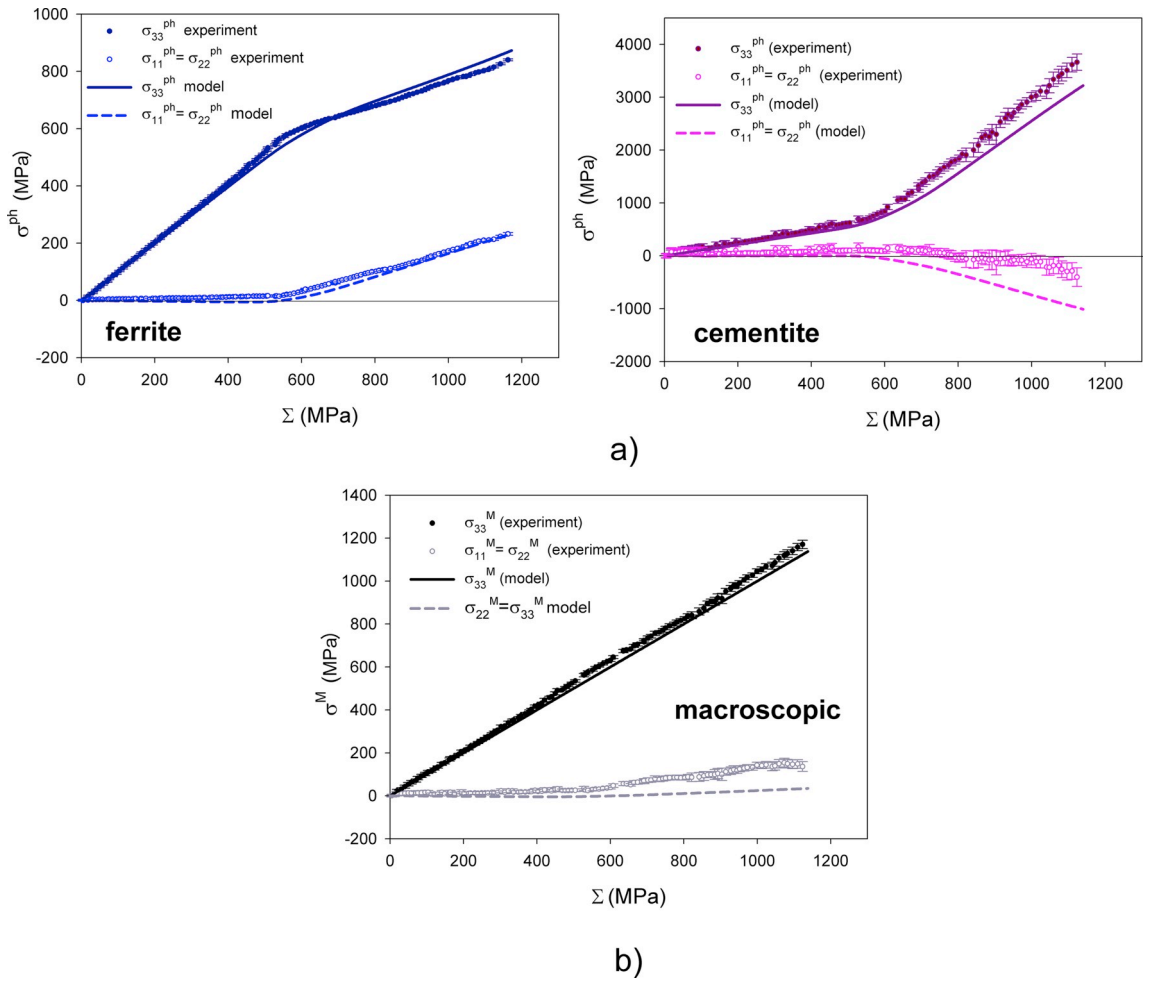

Fig. 9. Evolution of the phase stresses (a) and the overall stress (b) in specimen HT2 as a function of the applied macrostress. Experimental values (points) are compared with EPM model prediction (lines).

strain (Fig. 6 c, on the left), i.e. the stress heterogeneities occur at larger scale.

4.2. Stress evolution in the phases

The mean stresses in each phase, as well as the overall stress for the specimen HT2 were determined using the method presented in Appendix A, with the assumption of axial sample symmetry, i.e. $\sigma_{11}^{ph} = \sigma_{22}^{ph}$. The overall stress is defined as:

$$\sigma_{ii}^{M} = f\,\sigma_{ii}^{cem} + (1-f)\,\sigma_{ii}^{fer} \tag{12}$$

where f is the volume fraction of cementite and $i = 1,2$ or 3.

The evolution of the so obtained phase and overall stresses as a function of applied macroscopic stress are shown in Fig. 9. A very good agreement between the experiment and the model was found for the principal stresses in ferrite phase, while some deviation of the model from experimental data is observed for cementite, especially in the transverse direction (i.e. for $\sigma_{11}^{cem} = \sigma_{22}^{cem}$). This means that the model correctly predicts the lattice strains for ferrite not only in two directions (see previous chapter) but the agreement is also good for the stresses determined from $sin^2\psi$ plots, i.e. on the basis of many *hkl* reflections and orientations of the scattering vector (cf. Appendix A). The deviation of the corresponding plots in cementite is not large and is acceptable taking into account the experimental difficulties for this phase.

A very important conclusion can be made for the overall stress σ_{33}^{M} (in load direction) calculated from phase stresses using Eq. (12). It can be seen in Fig. 9 b, that the σ_{33}^{M} stress is approximately equal to the value of applied stress ($\sigma_{33}^{M} \approx \Sigma$). Also, the components $\sigma_{11}^{M} = \sigma_{22}^{M}$ are close to zero, with small deviation caused by some disagreement of the phase stress in cementite (see Fig. 9). Therefore, the

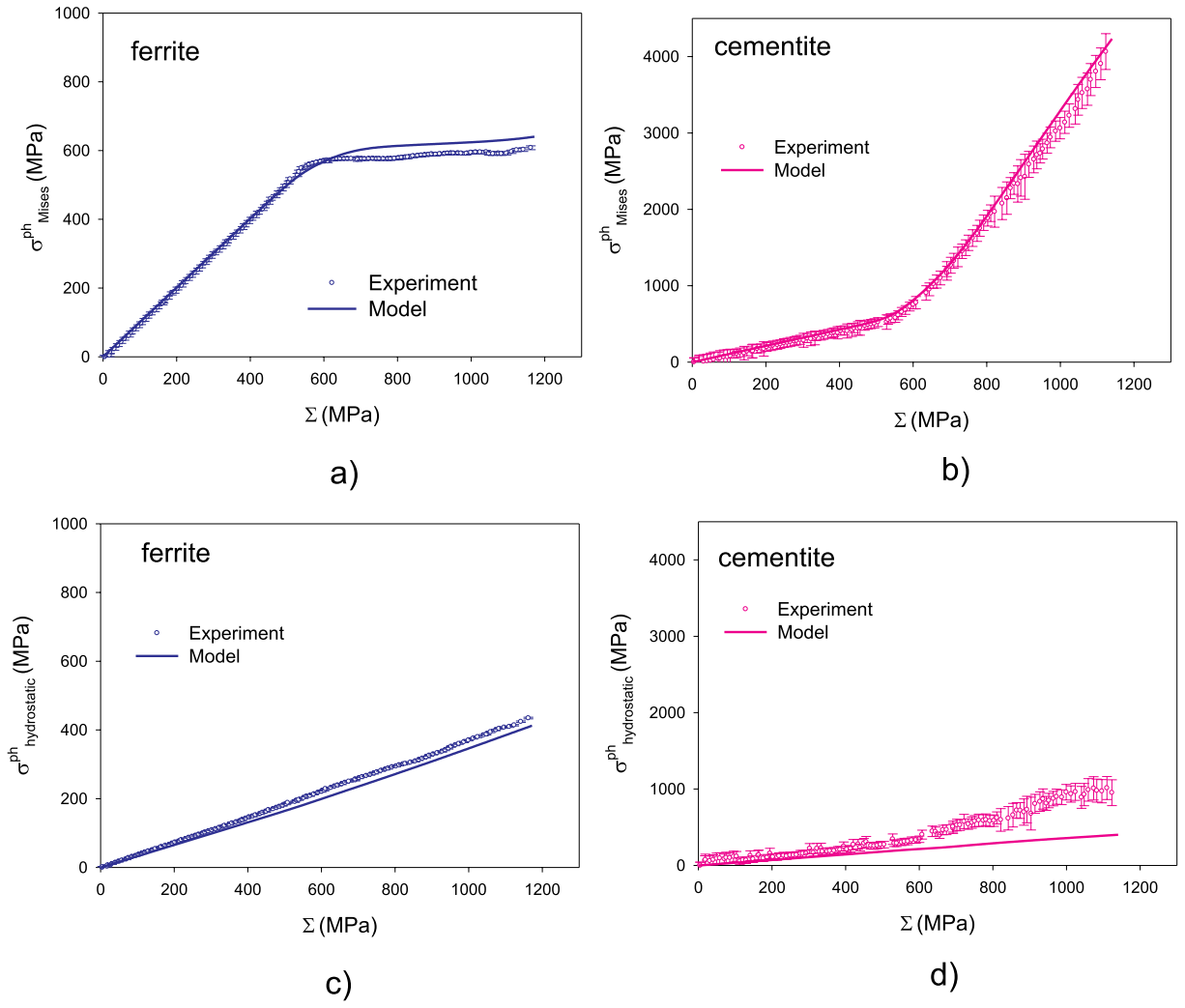

Fig. 10. Experimental (points) mean von Mises stress (a,b) and hydrostatic (c,d) stress in both phases of the HT2 specimen in relation to the applied macrostress, compared with EPM model predictions (lines).

mixture law defined by Eq. (12) is well fulfilled for the measured phase stresses (especially in the direction of applied load) and certainly it is fulfilled for the predicted stresses (see Fig. 9 b).

To analyse the elastoplastic process occurring in the phases, the von Mises and hydrostatic phase stresses were calculated from the measured and predicted mean σ_{ii}^{ph} values. The analysis of von Mises stress in the ferrite phase (shown in Fig. 10 a) leads to the conclusion that in the plastic range of deformation work hardening is not significant in the ferrite phase, so the main cause for macroscopic hardening is elastically deformed cementite, which accumulates very high stress. This conclusion is obviously confirmed by the model calculations in which the hardening parameter (θ_1^{fer}) was set to 50 *MPa*, see Table 5 (the theoretical values of von Mises stress are slightly overestimated). The von Mises stress for the cementite phase (Fig. 10 b) increases significantly in the plastic range of ferrite deformation, which is a consequence of the elastic nature of cementite deformation and its response for the plastic deformation of ferrite. The evolution of large von Mises stress in cementite agrees perfectly with the EPM model prediction (within the range of experimental uncertainty).

The observed low increase of von Mises stress in ferrite is caused by tensile stresses σ_{11}^{fer} and σ_{22}^{fer} (generated in ferrite due to the presence of cementite, see Fig. 9), which compensate an increase of σ_{33}^{fer}. It should be concluded that the coexistence of large von Mises stress in elastically deformed cementite and low von Mises stress in ferrite is possible due to the presence of interphase interaction in the transverse direction (i.e., presence of tensile stresses $\sigma_{11}^{fer} = \sigma_{22}^{fer}$ in ferrite).

Other interesting conclusions concern hydrostatic stresses. It can be assumed that the hydrostatic interphase stresses are not present in the initial sample and that the values assumed in data analysis as the stress free parameters are reasonable. As stated in the work of Young et al. (2007), the near-zero values of hydrostatic stresses can be related to two phenomena, which generate residual stresses in composite materials. The first reason is the mismatch in the thermal expansions coefficients of matrix and reinforcement which leads to compressive stress in cementite, and the second one is connected with the allotropic $\gamma - \alpha$ transformation of ferrite matrix which on the other hand generates the tensile stresses in the cementite phase (Basinski et al., 1955; Young et al., 2007). These two phenomena balance each other explaining the observed near zero stresses.

As shown in Fig. 10 c, a perfect agreement of the hydrostatic stress between the model and the experiment is observed in the ferrite phase. A high value of this stress is not limited by the ferrite yield threshold, since the hydrostatic stress does not affect the plastic deformation process. The hydrostatic stress corresponds only to the linear elastic deformation of the phases or generally of the material. Therefore the hydrostatic stresses should increase linearly also during plastic deformation, what is well seen in the case of ferrite phase. In the present experiment the hydrostatic stress in cementite does not agree well with the model prediction (cf. Fig. 11 d) but this stress is relatively small compared to the von Mises stress in this phase. It can be concluded that some disagreements of the principal stresses in cementite with the model prediction (cf. Fig. 8 a) are caused mostly by the deviation of experimental hydrostatic stress (Fig. 10 d), while the von Mises stress agrees very well with the model result (Fig. 10 b).

The estimation of the second-order stresses (see Appendix A) was also performed and root mean square values of stress tensor components for a statistical crystallite in the ferrite phase are shown in Fig. 11. The analysis revealed that the second-order stresses $\left(\sigma_{ij}^{II,\,fer}\right)$ were generated in ferrite only during its plastic deformation i.e. for applied stress over 500 *MPa*. It was observed that the values of σ_{ij}^{fer} determined from experimental data saturate at maximum values lower than 100 *MPa* (Fig. 11), i.e. they are much smaller than σ_{ij}^{fer} mean stress in ferrite (Fig. 9 a). It is also seen in Fig. 11 that the model predicted values of $\sigma_{ij}^{II,\,fer}$ are overestimated, especially in the direction of the applied load (x_3). The second-order stresses sum to zero value when the phase stresses σ_{ij}^{fer} are calculated over

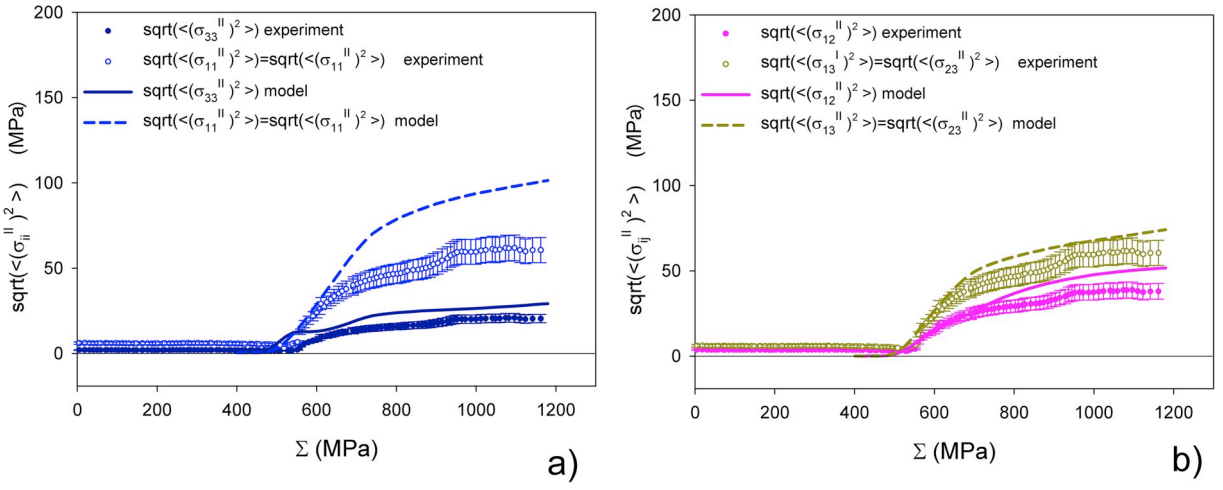

Fig. 11. Tensor components of experimental (points) second-order stress tensor in ferrite (HT2 specimen) as a function of the applied macrostress, compared with EPM model predictions (lines). The root mean square values are shown.

the ferrite phase. Although the values of $\sigma_{ij}^{II,\,fer}$ do not directly affect the average phase stresses, they influence the microscopic deformation at the scale of crystallites, and this effect is taken into account in model calculations. It should be emphasised that small second-order stresses were present also in ferrite, in the initial sample and during elastic deformation, however, the values of the initial second-order stresses caused by sample preparation cannot be determined by the method shown in Appendix A.

As mentioned above the cementite phase did not undergo plastic deformation, i.e. the incompatibility stresses in this phase were generated due to the interaction of elastic pearlite lamellae with the plastic matrix. It is interesting to notice the different behaviour of the $< a >_{\{hkl\}}$ vs. $sin^2\psi$ plots for both phases, corresponding to the different sources of the incompatibility stresses. Nonlinearities arise on the ferrite plots due to plastic anisotropy (Fig. A1) of ferrite crystallites, in which glides are activated on different slip systems. On the other hand for the elastic cementite the $< a >_{\{hkl\}}$ vs. $sin^2\psi$ plots remains linear (Fig. A1), but the slopes of these lines change due to differences in interaction of anisotropic elastic lamella with the plastic matrix. The latter phenomena is not well predicted by the model as shown in Appendix A.

4.3. Stress rate concentration tensor

The next step of the analysis concerned the localisation of stresses in both phases during elastoplastic deformation. The evolution of the stress localisation components (Eq. (10)) for the ferrite and cementite phases is shown in Fig. 12. In this figure the model predicted curves are also shown for the weighted model (EPM, Table 5) and the pure self-consistent model (EPSC). It can be concluded that in the elastic range of deformation the applied longitudinal stress $\Sigma_{33} = \Sigma$ localises in both phases equally (i.e., $B_{3333}^{fer} = B_{3333}^{cem} \approx 1$) and the transversal stresses are not generated ($B_{3311}^{fer} = B_{3311}^{cem} \approx 0$). Significant changes are observed at the beginning of the elastic-plastic transition, when the component B_{3333}^{ph}, responsible for the localisation of longitudinal stress, decreases in the ferrite phase and increases significantly in cementite (up to $B_{3333}^{cem}/B_{3333}^{fer} \approx 14.5$). This illustrates the partitioning of the stresses between phases, discussed above (cf. Figs. 9 and 10). On the other hand, the B_{3311}^{fer} component, responsible for the generation of the transverse stresses in ferrite, increases from zero to a positive value, causing the generation of tensile transverse stress. On the contrary, model calculations show a negative value of B_{3311}^{cem} for cementite, which should lead to equilibrium of stresses over both phases in the transverse direction. The latter prediction agrees qualitatively with the measurements, but in this case the experimental values are not accurately determined due to the low quality of the diffraction signal coming from the cementite (it was found that the phase stresses equilibrium condition was not fulfilled for their experimental values in the transverse direction - cf. discussion concerning Fig. 9). Finally, the stabilisation of all determined components is observed, which means that the stress localisation does not change significantly during advanced deformations. When the stabilisation of localisation occurs for two components and the B_{3333}^{ph} and B_{3311}^{ph} values approach each other for the ferrite phase (causing that von Mises stress does not arise in this phase, cf. Fig. 10 a) and diverge for cementite (leading to high von

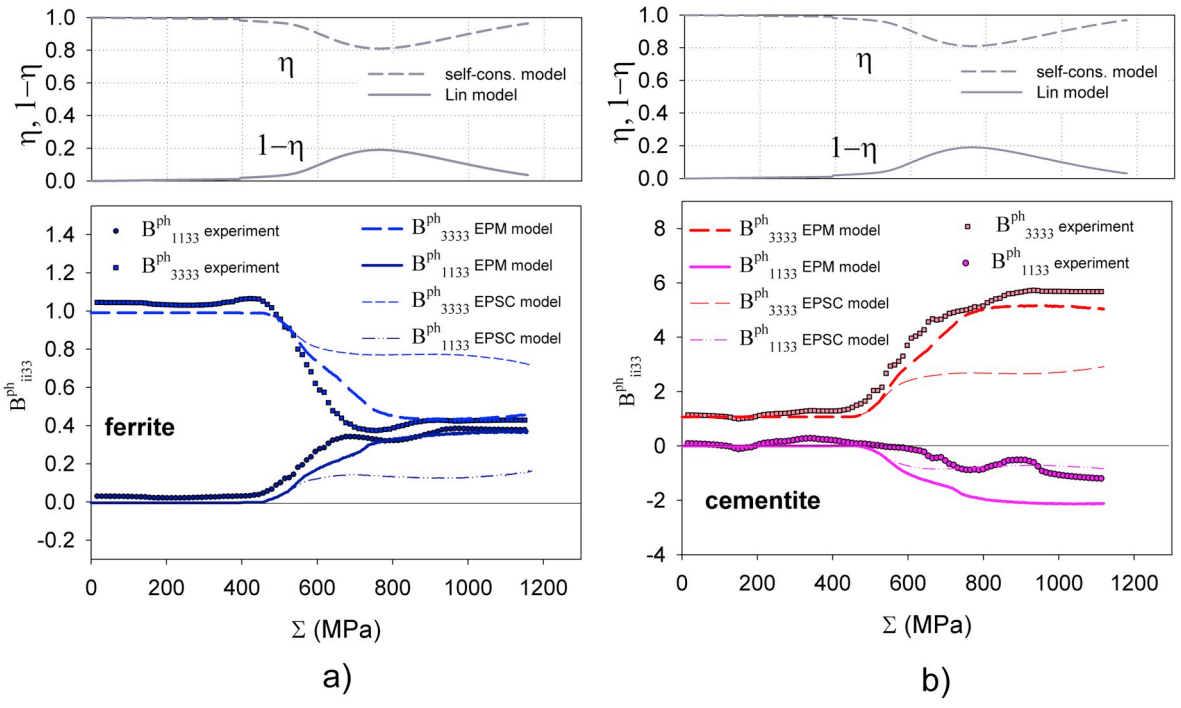

Fig. 12. Components of stress rate concentration tensor in ferrite (a) and cementite (b). Experimental (points) results for HT2 sample as a function of the applied macrostress are compared with EPM model and EPSC model predictions (lines).

Mises stress increase, cf. Fig. 10 b).

In the case of the EPM model, the predicted components B^{ph}_{33ii} of the localisation tensor agree well with the experimental results for the whole deformation range and for both phases, while the results obtained from the EPSC model are far from the experimental data during plastic deformation (cf. Fig. 12 b). The variation of η parameter (Fig. 12 a) indicates precisely when the localisation assumed in the EPM model differs from that predicted by the EPSC model, i.e. the contribution of the Lin's type interaction appears at the beginning of plastic deformation, while for the advanced sample strain (cf. also Fig. 9 a) this contribution decreases.

4.4. Reasons for the strengthening of perlite

The experimental data presented above allows us to discuss the main physical reasons for different initial hardness and very similar strain strengthening for the investigated samples. It was found that the initial CRSS for ferrite and yield stress of pearlite depend on the inter-lamellar spacings between cementite lamella, i.e. a smaller distance leads to a higher hardness of ferrite and, consequently, to a higher macroscopic yield stress of the steel (cf. τ_0^{fer} in Table 5 and the pearlite yield stresses in Fig. 6 b with interlamelar spacings given in Table 2 for HT1 and HT2 samples). This conclusion agrees with the previous experimental results (Allain and Bouaziz, 2008; Dollar et al., 1988; Yahyaoui et al., 2014) and is consistent with the empirical models proposed for lamellar pearlite given by Eq. (1) (Allain et al., 2019; Bouaziz and Le Corre, 2003). It should be emphasised that almost equal stress localisation in both phases during elastic deformation (i.e., $B^{fer}_{3333} = B^{cem}_{3333} \approx 1$ and $B^{fer}_{3311} = B^{cem}_{3311} \approx 0$) causes that the effect of stress transition between phases is not significant and the mean stresses are approximately equal in ferrite and cementite. In this case, the plastic flow of pearlite is controlled only by the hardness of the ferrite, which is related to the thickness of ferrite lamellae (the size effect). This type of material strengthening depends on the dislocation interactions with the ferrite-cementite interphase boundaries. Hence, the dislocation density and spatial distribution significantly affect the initial yield of the ferrite phase and, consequently, the initial yield of pearlite, as determined by Yahyaoui et al. (2014).

It was found that during plastic deformation large stresses are concentrated in cementite ($B^{cem}_{3333}/B^{fer}_{3333} \rightarrow 14.5$) causing important strain strengthening of the pearlite. This is caused by a large difference in the tangent moduli of elastically stiff cementite and soft, plastically deformed ferrite. The roles of cementite and ferrite in material strengthening can be studied on the basis of the von Mises stress evolution determined in both phases. In the range of plastic deformation the mean von Mises stress in ferrite (being a measure of yield stress evolution for this phase) does not change significantly due to a small work hardening of this phase. As noticed above, the low and stable value of the ferrite yield stress is possible due to the increase of tensile stress generated in this phase, in the direction perpendicular to the applied load. The evolution of the measured phase stresses and the corresponding macrostress (calculated from Eq. (12)) directly showed that the increase of the overall strength of lamellar pearlite during elastoplastic deformation comes mostly from the extraordinary value of stress concentrated in elastically deformed cementite. The total stress practically does not depend on the comparatively slight increase in the stress in ferrite (cf. Figs. 9 and 10). This means that the effect of stress distribution between the phases during plastic deformation dominated the effects associated with the dislocation hardening of ferrite, and as a consequence interlamelar spacings do not significantly affect the yield stress evolution of fully lamellar pearlite. Measurements of phase stresses and their analysis explained the surprising experimental result showing that the deformation strengthening of fully lamellar pearlite does not depend on the inter-lamellar distances. This effect was observed by many authors (Allain and Bouaziz, 2008; Dollar et al., 1988; Yahyaoui et al., 2014) and it was also incorporated into the empirical hardening law (Bouaziz and Le Corre, 2003). It should be emphasised that, unlike fully lamellar pearlite, in other pearlitic steels, e.g. ferrite–pearlite steel (Allain and Bouaziz, 2008) or globular pearlitic steel (Allain et al., 2019), the sizes of pearlite or cementite grains significantly affect the strain strengthening of the material.

5. Summary

Synchrotron X-ray diffraction measurements were used to study the evolution of lattice strain and stresses in both phases of C70 fully pearlitic steel during an elastoplastic *in situ* tensile test. The evolution of the components of the stress rate concentration tensor showed approximately equal stress localisation in the cementite and ferrite phases during elastic deformation, an important change of stress localisation during elastic-plastic transition, and finally stable and significantly higher localisation of stresses in cementite compared to ferrite during advanced plastic deformation.

The distribution of stresses between the phases has a significant impact on the type of reinforcement of fully lamellar pearlite. The initial yield strength is affected only by the hardness of the ferrite (depending on inter-lamellar spacings), because equal stresses are located in both phases. However, during plastic deformation, the transfer of stress from ferrite to cementite (a process independent of inter-lamellar spacing) dominates in the strain strengthening of pearlite, therefore the effect of the low hardness of ferrite is not significant. The obtained results explain the experimental observations presented by many authors for completely lamellar pearlite.

In elasticity, the lattice strains measured for different crystallite groups (selected by different *hkl* reflections) agree with these predicted by EPSC model, but it was found that this model does not correctly predict the partitioning of the lattice strains and stresses between phases during the plastic deformation of pearlite. The diffraction results, as well as macroscopic mechanical behaviour, were much better reproduced by the proposed intermediate EPM model, in which contributions of the stress localisation calculated on the basis of the self-consistent and Lin models were varied during plastic deformation.

The second-order stresses were observed in this phase in the initial and elastically deformed samples, but these stresses are replaced by plastic incompatibility stresses in the beginning of plastic deformation. The latter stresses were quantitatively determined in the ferrite phase and they are much smaller than the mean phase stress. Insignificant second-order stresses were detected in cementite,

which remains elastic during the whole range of deformation.

Finally, it was found that the lattice strains measured in cementite do not agree with the EPM model for a relatively large sample strain. Experimental data show a relaxation of the load in this phase and this effect can be explained by the fracturing of the cementite lamellae.

Declaration of competing interest

The authors declare that they have no known competing financial interests or personal relationships that could have appeared to influence the work reported in this paper.

CRediT authorship contribution statement

E. Gadalińska: Investigation, Formal analysis, Software, Writing - original draft. **A. Baczmański:** Conceptualization, Methodology, Software, Formal analysis, Writing - review & editing, Supervision. **C. Braham:** Conceptualization, Methodology, Investigation, Supervision. **G. Gonzalez:** Formal analysis, Software, Methodology. **H. Sidhom:** Conceptualization, Resources, Writing - original draft. **S. Wroński:** Investigation, Software, Formal analysis. **T. Buslaps:** Investigation. **K. Wierzbanowski:** Formal analysis, Writing - review & editing.

Acknowledgements

This work was supported by the National Science Centre, Poland (NCN), under grant No. UMO-2017/25/B/ST8/00134. We acknowledge the European Synchrotron Radiation Facility (ESRF) for the provision of synchrotron radiation facilities in the framework of the MA 1611.

Appendix A

The normal components of the stress tensors σ_{ii}^{ph} were determined independently for each phase using the multireflection method (Baczmanski et al., 2008; Wroński et al., 2007). In analysis the X-ray stress factors were calculated from single-crystal elastic constants (SEC) given in Table 4, using the Eshelby-Kröner model with the assumption of non-textured material (Baczmanski et al., 2008).

Additionally, in the case of the ferrite phase the second-order plastic incompatibility stresses $\sigma_{ij}^{II,\,ph}$ generated during the tensile test were evaluated (Wawszczak et al., 2016; Wroński et al., 2007). The latter stresses describe fluctuation around a mean phase stress σ_{ij}^{ph} due to differences in plastic deformation of crystallites having different lattice orientations. It can be shown, that for non-textured material the $< a >_{\{hkl\}}$ vs. $sin^2\psi$ plots (ψ angle is defined in Fig. 2) exhibit linear character, when only the phase stresses (σ_{ii}^{ph}) are present, while the second order stresses $\sigma_{ij}^{II,\,ph}$ in plastically deformed phase cause nonlinearities of these plots (Baczmanski et al., 2008).

The above stress analysis was used to determine the principal stresses σ_{ii}^{ph} in cementite and ferrite during a tensile test performed for a pearlitic sample (Fig. 9), assuming axial symmetry around x_3 axis (i.e. $\sigma_{11}^{ph} = \sigma_{22}^{ph}$). This assumption is reasonable because of the random crystallographic texture and the fact that uniaxial stress was applied along axis x_3. For a given phase, the theoretical lines were fitted simultaneously to all $< a >_{\{hkl\}}$ values measured with different reflections (cf. Table 3) and scattering vector orientations (i.e. different ψ, cf. Fig. 2), as presented in Figs. A1 and A.2. It should be stated, that analysis of $\sigma_{ij}^{II,\,ph}$ stresses based on non-linearity of $< a >_{\{hkl\}}$ vs. $sin^2\psi$ is applicable only for ferrite which is subjected to plastic deformation.

At first the stress analysis was done for the initial sample assuming additionally that the hydrostatic stresses in both phases are equal to zero (Young et al., 2007), and as a result, negligible stresses were found in ferrite ($\sigma_{11}^{fer} = \sigma_{22}^{fer} = 6.3 \pm 3.2$ MPa and $\sigma_{33}^{fer} = 12.6 \pm 2.7$ MPa), as well as in cementite ($\sigma_{11}^{cem} = \sigma_{22}^{cem} = 16.6 \pm 18.8$ MPa and $\sigma_{33}^{cem} = -11.8 \pm 15.2$ MPa). Because the stresses in both phases are very small, the stress free lattice parameters (Table 3) were determined for both phases from diffraction data obtained for the initial sample. These stress free lattice parameters were then used in stress analysis performed for the loaded sample. The results of this analysis are shown in Fig. 9 (phase stresses) and Fig. 11 (second-order stresses).

As seen in Fig. A1, small nonlinearities exist on the $< a >_{\{hkl\}}$ vs. $sin^2\psi$ plot for ferrite in the initial sample and the same character of nonlinearities remains unchanged for elastically deformed sample (cf. $\Sigma = 508\ MPa$). However, the origin of these nonlinearities is unknown, and they are not correlated with model prediction done for tensile test. As a result a value close to zero of $\sigma_{ij}^{II,\,ph}$ was obtained for the initial, as well as the elastically deformed sample (Fig. 11). For the advanced plastic deformation of ferrite (cf. $\Sigma = 914\ MPa$) the plots are also non-linear but the character of the deviations is different (smooth curvature appeared). The curvatures of the $< a >_{\{hkl\}}$ vs. $sin^2\psi$ plots are well matched by the theoretical lines. As a result, increasing second-order stresses $\sigma_{ij}^{II,\,ph}$ with subsequent saturation were found during plastic deformation (Fig. 11).

In the case of elastic cementite the $< a >_{\{hkl\}}$ vs. $sin^2\psi$ plots are linear, but the trends of the experimental points are correlated with the slope of the predicted line for the individual *hkl* reflections only during elastic deformation (cf. plot $\Sigma = 508$ MPa in Fig. A2 a,b). During plastic deformation, the experimental plots are still linear but there are not well correlated with the theoretical lines. However,

if the differences between the *hkl* reflection are neglected, it can be concluded that theoretical lines in general fit well to the experimental data (cf. plot $\Sigma = 914$ MPa in Fig. A2 c,d).

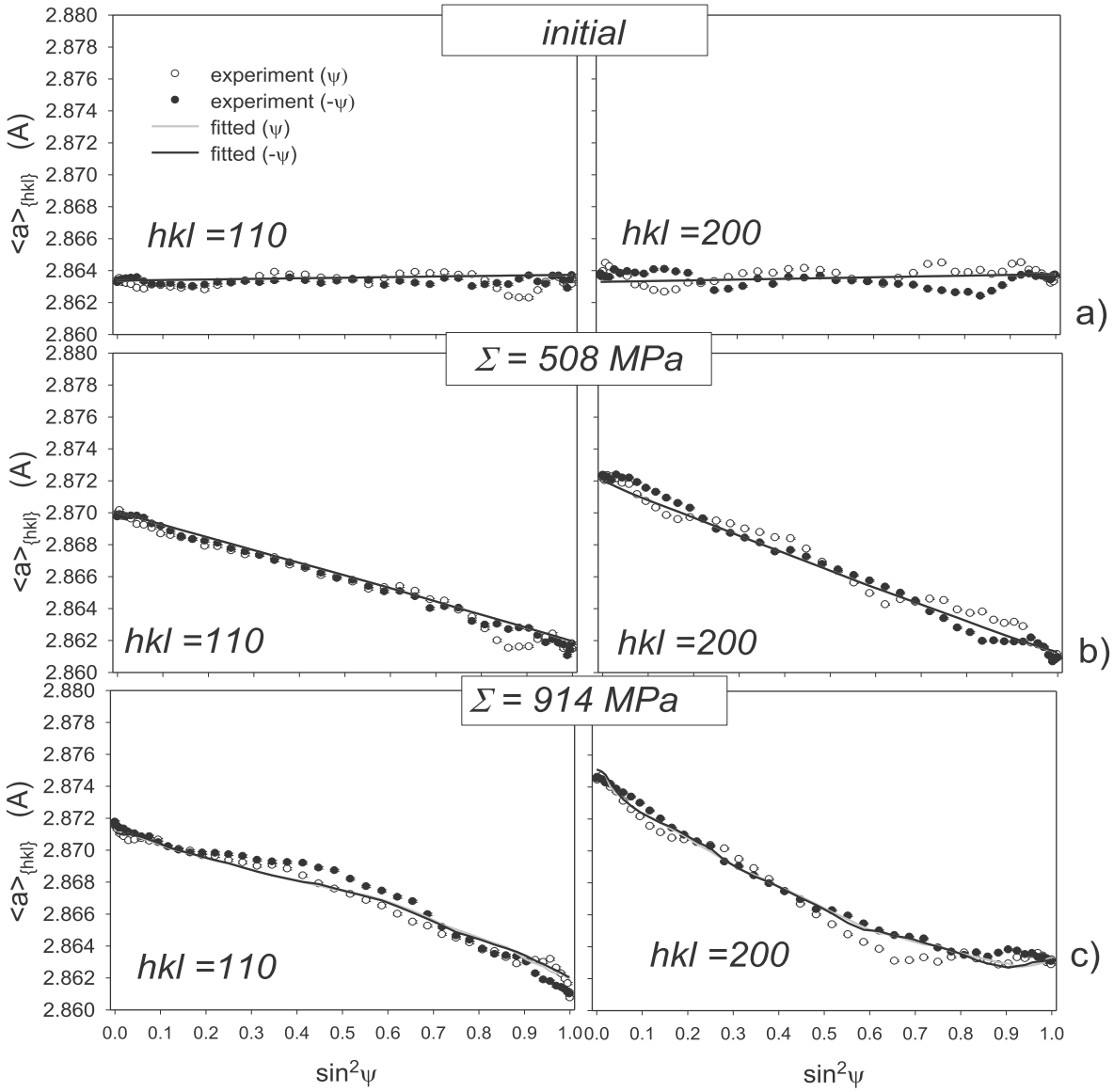

Fig. A1. The example $sin^2\psi$ plots for ferrite measured with step of $\Delta\psi = 2^\circ$ for the initial (a) and loaded sample HT2: $\Sigma = 508$ MPa (b) and $\Sigma = 914$ MPa (c). Results are shown for two sets of inclination angles (defined in Fig. 2): $+\psi$ and $-\psi$. The fitted lines correspond to the determined stresses.

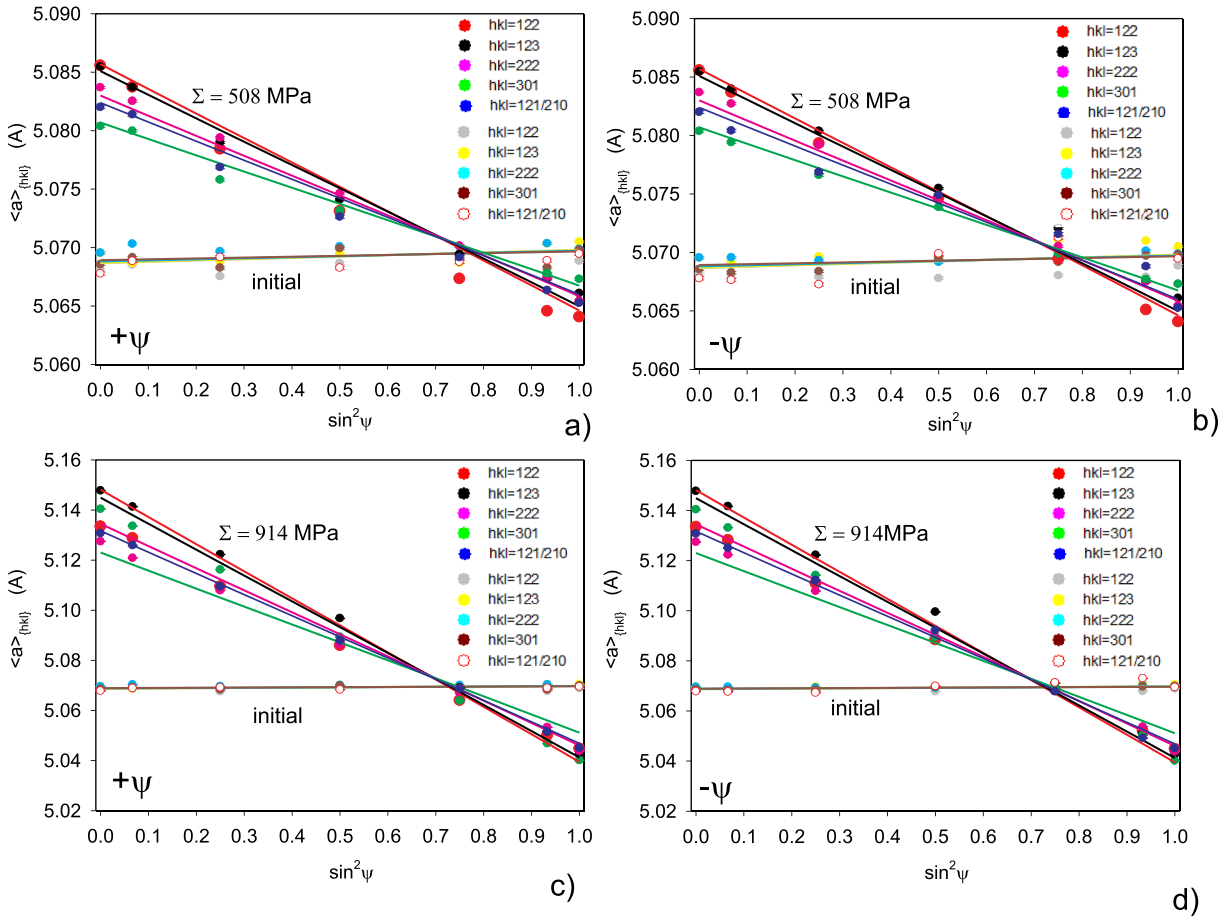

Fig. A2. The $sin^2\psi$ plots for cementite measured with step of $\Delta\psi = 15^\circ$ for the initial and loaded sample HT2: $\Sigma = 508$ MPa (a,b) and $\Sigma = 914$ MPa (b,c). Results are shown for two sets of inclination angles (defined in Fig. 2): $+\psi$ (a,c) and $-\psi$ (b,d). The fitted lines correspond to the determined stresses (notice very different vertical scales between a,b and c,d).

Appendix B

The principles of the EPM method allowing the quantitative description of a deviation of the experimental results from the EPSC model are presented below. This method is based on the η and ξ parameters used to tune model prediction to experimental results and it can be easily incorporated into the EPSC algorithm.

a) Principles of homogenisation

In homogenisation procedures used to describe the elastic or elastoplastic (tangential) behaviour of polycrystalline materials, a homogenous medium equivalent to the considered RVE (representative volume element) of polycrystal is considered. It can be shown that in the case of homogenous boundary conditions the stress and strain applied to the sample ($\boldsymbol{\Sigma}$ and $\boldsymbol{E}$) are equal to the volume averages, calculated for local values $\boldsymbol{\sigma} = \boldsymbol{\sigma}(\boldsymbol{x})$ and $\boldsymbol{\varepsilon} = \boldsymbol{\varepsilon}(\boldsymbol{x})$ over the RVE (Bishop and Hill, 1951; Hill, 1967; Mandel, 1966; Morawiec, 2004), i.e.:

$$\boldsymbol{\Sigma} = \frac{1}{V}\int_V \boldsymbol{\sigma}\, dV = <\boldsymbol{\sigma}> \quad \text{and} \quad \boldsymbol{E} = \frac{1}{V}\int_V \boldsymbol{\varepsilon}\, dV = <\boldsymbol{\varepsilon}> \tag{B.1}$$

The mean specific energy and Hook's law can be expressed through the averages defined above and the effective macroscopic stiffness tensor $\boldsymbol{C}$, i.e.:

$$<U> = <\boldsymbol{\varepsilon}>\boldsymbol{C}<\boldsymbol{\varepsilon}>/2 \quad \text{and} \quad <\boldsymbol{\sigma}> = \boldsymbol{C}<\boldsymbol{\varepsilon}> \tag{B.2}$$

For homogenous boundary conditions, the effective moduli must fulfil the equivalence energy principle (Hill-Mandel's lemma (Bishop and Hill, 1951; Hill, 1967; Mandel, 1966; Morawiec, 2004):

$$2<U>=<\boldsymbol{\varepsilon}\boldsymbol{\sigma}>=<\boldsymbol{\varepsilon}>\boldsymbol{C}<\boldsymbol{\varepsilon}>=<\boldsymbol{\varepsilon}><\boldsymbol{\sigma}> \tag{B.3}$$

which leads to definitions of effective modulus given through relationships:

$$\boldsymbol{C}<\boldsymbol{\varepsilon}>=<\boldsymbol{c}\boldsymbol{\varepsilon}> \quad \text{or} \quad <\boldsymbol{\varepsilon}>\boldsymbol{C}<\boldsymbol{\varepsilon}>=<\boldsymbol{\varepsilon}\boldsymbol{c}\boldsymbol{\varepsilon}> \tag{B.4}$$

where the local Hook's law is written using the local modulus $\boldsymbol{\sigma} = \boldsymbol{c}\boldsymbol{\varepsilon}$.

If we define the local strain $\boldsymbol{A}$ and stress $\boldsymbol{B}$ concentration tensors through:

$$\boldsymbol{\varepsilon} = \boldsymbol{A}\boldsymbol{E} = \boldsymbol{A}<\boldsymbol{\varepsilon}> \quad \text{and} \quad \boldsymbol{\sigma} = \boldsymbol{B}\boldsymbol{\Sigma} = \boldsymbol{B}<\boldsymbol{\sigma}> \tag{B.5}$$

the effective modulus (consistent with Hill-Mandel's lemma and Eq. (B.1)) can be computed from one of the equations:

$$\boldsymbol{C} = <\boldsymbol{c}\boldsymbol{A}> \quad \text{or} \quad \boldsymbol{C} = <\boldsymbol{A}^{-1}\boldsymbol{c}\boldsymbol{A}> \tag{B.6a}$$

or, alternatively from

$$\boldsymbol{C} = <\boldsymbol{c}^{-1}\boldsymbol{B}>^{-1} \quad \text{or} \quad \boldsymbol{C} = <\boldsymbol{B}^{-1}\boldsymbol{c}^{-1}\boldsymbol{B}>^{-1} \tag{B.6b}$$

Similar description can be used in the case of incremental models of plastic deformation in which constant tangent moduli are used within small increments of deformation (Bishop and Hill, 1951; Hill, 1967). In this case, the stress and strain rates denoted by dot can be related through a local tangent modulus $\boldsymbol{l}$ or an overall tangent modulus $\boldsymbol{L}$:

$$\dot{\boldsymbol{\sigma}} = \boldsymbol{l}\dot{\boldsymbol{\varepsilon}} \quad \text{and} \quad \dot{\boldsymbol{\Sigma}} = <\dot{\boldsymbol{\sigma}}> = \boldsymbol{L}<\dot{\boldsymbol{\varepsilon}}> = \boldsymbol{L}\dot{\boldsymbol{E}} \tag{B.7}$$

and the effective tangent modulus $\boldsymbol{L}$ tensor can be calculated from:

$$\boldsymbol{L} = <\boldsymbol{l}\boldsymbol{A}> \quad \text{or} \quad \boldsymbol{L} = <\boldsymbol{A}^{-1}\boldsymbol{l}\boldsymbol{A}> \tag{B.8a}$$

or, alternatively from

$$\boldsymbol{L} = <\boldsymbol{l}^{-1}\boldsymbol{B}>^{-1} \quad \text{or} \quad \boldsymbol{L} = <\boldsymbol{B}^{-1}\boldsymbol{l}^{-1}\boldsymbol{B}>^{-1} \tag{B.8b}$$

b) **Lipinski-Berveiller model and scaling parameters**

In this work the EPSC (elastoplastic self-consistent) incremental model proposed by Lipinski and Berveiller (1989) and Lipinski et al. (1995) and its modification are used to predict elastoplastic deformation of pearlite. The polycrystalline grains (crystallites) are represented by ellipsoidal Eshelby inclusions (Eshelby, 2007), numbered by i, for which the strain rate concentration tensor is given by the equation:

$$\boldsymbol{A}^i_{sc} = \left(\boldsymbol{I} - \boldsymbol{T}^{ii}_{sc}\Delta\boldsymbol{l}^i_{sc}\right)^{-1} \quad \text{and} \quad \boldsymbol{B}^i_{sc} = \boldsymbol{l}^i_{sc}\boldsymbol{A}^i_{sc}\boldsymbol{L}^{-1}_{sc} \tag{B.9}$$

where $\Delta\boldsymbol{l}^i_{sc} = \boldsymbol{l}^i - \boldsymbol{L}_{sc}$, $\boldsymbol{T}^{ii}_{sc} = \boldsymbol{S}^i_{sc}\boldsymbol{L}^{-1}_{sc}$ is the interaction tensor expressed by Eshelby tensor $\boldsymbol{S}^i_{sc}$ and effective tangent moduli tensor $\boldsymbol{L}_{sc}$, while $\boldsymbol{I}$ is the fourth rank unit tensors (for details see Lipinski et al., 1995; Lipinski and Berveiller, 1989).

The effective moduli are calculated according to the first of Eqs. B.8a and B.8b, which take form of a sum over all considered inclusions:

$$\boldsymbol{L}_{sc} = <\boldsymbol{l}^i\boldsymbol{A}^i_{sc}>_N = \frac{1}{N}\sum_i^N \boldsymbol{l}^i\boldsymbol{A}^i_{sc} \quad \text{or} \quad \boldsymbol{L}^{-1}_{sc} = <\left(\boldsymbol{l}^{-1}\right)^i\boldsymbol{B}^i_{sc}>_N = \frac{1}{N}\sum_i^N \left(\boldsymbol{l}^{-1}\right)^i\boldsymbol{B}^i_{sc} \tag{B.10}$$

If the experimental data deviate from the model results, the observed discrepancy should be described quantitatively. To do this, we propose the parameters $\eta \in [0,1]$ and $\xi \in [0,1]$, which determine the distances of the experimental results from the self-consistent model ($\eta = \xi = 1$) toward the Lin/Voigt models ($\eta = 0$; assuming homogenous total strain $\dot{\boldsymbol{\varepsilon}}^i_{sc} = \dot{\boldsymbol{E}}$ (Lin, 1957; Voigt, 1928) or toward the Sachs/Reuss models ($\xi = 0$; assuming homogenous stress $\dot{\boldsymbol{\sigma}}^i_{sc} = \dot{\boldsymbol{\Sigma}}$ (Reuss, 1929; Sachs, 1928), respectively. The dependence of the model type on the η and ξ values is visualised in Fig. B1. The parameter η (or ξ) proportionally reduces the fluctuations of local strain rates $\dot{\boldsymbol{\varepsilon}}^i_{sc}$ (or local stress rates $\dot{\boldsymbol{\sigma}}^i_{sc}$) around the average value $<\dot{\boldsymbol{\varepsilon}}^i_{sc}>_N = \dot{\boldsymbol{E}}$ (or $<\dot{\boldsymbol{\sigma}}^i_{sc}>_N = \dot{\boldsymbol{\Sigma}}$), predicted by the self-consistent model, i.e.:

$$\left(\dot{\boldsymbol{\varepsilon}}^i - \dot{\boldsymbol{E}}\right) = \eta\left(\dot{\boldsymbol{\varepsilon}}^i_{sc} - \dot{\boldsymbol{E}}\right) \quad \text{for} \quad \eta \in [0,1] \text{ or } \left(\dot{\boldsymbol{\sigma}}^i - \dot{\boldsymbol{\Sigma}}\right) = \xi\left(\dot{\boldsymbol{\sigma}}^i_{sc} - \dot{\boldsymbol{\Sigma}}\right) \quad \text{for} \quad \xi \in [0,1] \tag{B.11}$$

where $\dot{\boldsymbol{\varepsilon}}^i$ and $\dot{\boldsymbol{\sigma}}^i$ correspond to the given scaling parameters η and ξ.

Substituting relations $\dot{\boldsymbol{\varepsilon}}^i = \boldsymbol{A}^i_\eta\dot{\boldsymbol{E}}$ and $\dot{\boldsymbol{\varepsilon}}^i_{sc} = \boldsymbol{A}^i_{sc}\dot{\boldsymbol{E}}$ (or $\dot{\boldsymbol{\sigma}}^i = \boldsymbol{B}^i\dot{\boldsymbol{\Sigma}}$ and $\dot{\boldsymbol{\sigma}}^i_{sc} = \boldsymbol{B}^i_{sc}\dot{\boldsymbol{\Sigma}}$) the localisation tensor for a given η (or ξ) can be constructed:

$$\boldsymbol{A}^i_\eta = \eta\left(\boldsymbol{A}^i_{sc} - \boldsymbol{I}\right) + \boldsymbol{I} = \eta\boldsymbol{A}^i_{sc} + (1-\eta)\boldsymbol{I} \quad \text{for} \quad \eta \in [0,1] \text{ or } \boldsymbol{B}^i_\xi = \xi\left(\boldsymbol{B}^i_{sc} - \boldsymbol{I}\right) + \boldsymbol{I} = \xi\boldsymbol{B}^i_{sc} + (1-\xi)\boldsymbol{I} \quad \text{for} \quad \xi \in [0,1] \tag{B.12}$$

Therefore, the effective tangent moduli calculated from Eq. (B.10) are:

$$\boldsymbol{L}_{\eta} = <\boldsymbol{l}^{i}\boldsymbol{A}_{\eta}^{i}>_{N} = \eta <\boldsymbol{l}^{i}\boldsymbol{A}_{sc}^{i}>_{N} + <\boldsymbol{l}^{i}>_{N} - \eta <\boldsymbol{l}^{i}>_{N} = \eta\boldsymbol{L}_{sc} + (1-\eta)\,\boldsymbol{L}_{TV} \text{ or } \boldsymbol{L}_{\xi}^{-1} = <\left(\boldsymbol{l}^{-1}\right)^{i}\boldsymbol{B}_{\xi}^{i}>_{N} = \xi\boldsymbol{L}_{sc}^{-1} + (1-\xi)\,\boldsymbol{L}_{SR}^{-1} \tag{B.13}$$

where $\boldsymbol{L}_{LV} = <\boldsymbol{l}^{i}>_{N}$ is the Lin/Voigt arithmetical mean corresponding to the assumption of homogenous total strain field (i.e. $\dot{\boldsymbol{\varepsilon}}^{i} = \dot{\boldsymbol{E}}$), and $\boldsymbol{L}_{SR}^{-1} = <\left(\boldsymbol{l}^{-1}\right)^{i}>_{N}$ is the Sachs/Reuss harmonic mean corresponding to the assumption of a homogenous stress field (i.e. $\dot{\boldsymbol{\sigma}}^{i} = \dot{\boldsymbol{\Sigma}}$).

The so calculated tangent modulus tensor $\boldsymbol{L}_{\eta}$ is between that obtained from the self-consistent model ($\boldsymbol{L}_{\eta} = \boldsymbol{L}_{sc}$ for $\eta = 1$) and the Lin/Voigt upper bound ($\boldsymbol{L}_{\eta} = \boldsymbol{L}_{LV}$ for $\eta = 0$), while the $\boldsymbol{L}_{\xi}$ tangent modulus tensor is between the one obtained from the self -consistent model ($\boldsymbol{L}_{\xi} = \boldsymbol{L}_{sc}$ for $\xi = 1$) and the lower bound determined by the Sachs/Reuss assumption ($\boldsymbol{L}_{\xi} = \boldsymbol{L}_{SR}$ for $\xi = 0$), i.e.:

$$\boldsymbol{L}_{LV} \geq \boldsymbol{L}_{\eta} \geq \boldsymbol{L}_{sc} \quad \text{and} \quad \boldsymbol{L}_{sc} \geq \boldsymbol{L}_{\xi} \geq \boldsymbol{L}_{SR} \tag{B.14}$$

c) Hill's approach and the simplified Zaoui-Berveiller model

Alternatively, the deviation from the self-consistent model can be quantitatively described using Hill's constitutive equation (equivalent to the Lipinski-Berveiller model, but with the assumption of equal interaction tensor $\boldsymbol{T}_{sc}^{ii}$ for all inclusions). Hill's equation (Hill, 1965) can be written for the case of a self-consistent model and then the strain or stress fluctuation field can be modified using Eq. (B.11):

$$\begin{aligned}\left(\dot{\boldsymbol{\sigma}}^{i} - \dot{\boldsymbol{\Sigma}}\right) &= \boldsymbol{L}_{sc}^{*}\left(\dot{\boldsymbol{E}} - \dot{\boldsymbol{\varepsilon}}_{sc}^{i}\right) = 1\Big/\eta\,\boldsymbol{L}_{sc}^{*}\left(\dot{\mathbf{E}} - \dot{\boldsymbol{\varepsilon}}^{i}\right) \quad \text{for} \quad \eta \in [0,1] \text{ or } \left(\dot{\boldsymbol{\varepsilon}}^{i} - \dot{\boldsymbol{E}}\right) = \left(\boldsymbol{L}_{sc}^{*}\right)^{-1}\left(\dot{\boldsymbol{\Sigma}} - \dot{\boldsymbol{\sigma}}_{sc}^{i}\right) \\ &= 1\Big/\xi\left(\boldsymbol{L}_{sc}^{*}\right)^{-1}\left(\dot{\boldsymbol{\Sigma}} - \dot{\boldsymbol{\sigma}}_{sc}^{i}\right) \quad \text{for} \quad \xi \in [0,1]\end{aligned} \tag{B.15}$$

where $\boldsymbol{L}_{sc}^{*} = \left(\boldsymbol{T}_{sc}^{ii}\right)^{-1} - \boldsymbol{L}_{sc} = \boldsymbol{L}_{sc}\left(\left(\boldsymbol{S}_{sc}^{i}\right)^{-1} - \boldsymbol{I}\right)$ is the Hill's constrain tensor and $\boldsymbol{S}_{sc}^{i}$ is the Eshelby tensor for elastoplastic effective medium characterised by tangent modulus tensor $\boldsymbol{L}_{sc}$.

The latter equations can be rewritten in another form:

$$\left(\dot{\boldsymbol{\sigma}}^{i} - \dot{\boldsymbol{\Sigma}}\right) = \alpha_{H}\,\boldsymbol{L}_{sc}^{*}\left(\dot{\mathbf{E}} - \dot{\boldsymbol{\varepsilon}}^{i}\right) \tag{B.16}$$

where $\alpha_{H} = 1/\eta \in [1,\infty)$ and $\alpha_{H} = \xi \in [0,1]$, i.e. $\alpha_{H} \in [0,\infty)$.

This equivalent approach leads directly to the well-known simplified Berveiller and Zaoui (1978) model when two significant assumptions are introduced: instead of effective tangent modulus, the isotropic elastic tensor of macroscopic stiffness is used in the calculation of Hill's constrain tensor, i.e. $\boldsymbol{L}_{sc}^{*} = \boldsymbol{C}_{iso}\left(\left(\boldsymbol{S}^{i}\right)^{-1} - \boldsymbol{I}\right)$, where the Eshelby tensor $\boldsymbol{S}^{i}$ is calculated for spherical inclusion embedded in isotropic elastic matrix. Assuming proportional loading and using a secant "isotropization" method the constitutive relation given by Eq. (B.16) was simplified (Berveiller and Zaoui, 1978). For given Poisson's ratio ν and shear modulus μ it can be written:

$$\left(\dot{\boldsymbol{\sigma}}^{i} - \dot{\boldsymbol{\Sigma}}\right) = 2\alpha(1-\beta)\mu\left(\dot{\boldsymbol{E}}^{pl} - \left(\dot{\boldsymbol{\varepsilon}}^{pl}\right)^{i}\right) \quad \text{for} \quad \alpha \in [0,2] \tag{B.17}$$

where $\beta = 2(4-5\nu)/15(1-\nu)$, $\dot{\boldsymbol{E}}^{pl}$ and $\dot{\boldsymbol{\varepsilon}}^{pl}$ are the macroscopic and grain plastic strain rates, respectively.

The equation above was proposed by Berveiller and Zaoui (1978) in an integrated form (without dots) for constant α, μ and ν.

References

Adamczyk-Cieślak, B., Koralnik, M., Kuziak, R., Brynk, T., Zygmunt, T., Mizera, J., 2019. Low-cycle fatigue behaviour and microstructural evolution of pearlitic and bainitic steels. Mater. Sci. Eng. A 747, 144–153. https://doi.org/10.1016/j.msea.2019.01.043.

Agnew, S.R., Singh, A., Calhoun, C.A., Mulay, R.P., Bhattacharyya, J.J., Somekawa, H., Mukai, T., Clausen, B., Wu, P.D., 2018. In-situ neutron diffraction of a quasicrystal-containing Mg alloy interpreted using a new polycrystal plasticity model of hardening due to {10.2} tensile twinning. Int. J. Plast. https://doi.org/10.1016/j.ijplas.2017.09.005.

Allain, S., Bouaziz, O., 2008. Microstructure based modeling for the mechanical behavior of ferrite-pearlite steels suitable to capture isotropic and kinematic hardening. Mater. Sci. Eng. A 496, 329–336. https://doi.org/10.1016/j.msea.2008.06.009.

Allain, S.Y.P., Roth, A., Bouaziz, O., D'Eramo, E., 2019. Microstructure-based behavior law for globular pearlitic steels. J. Mater. Res. Technol. 8, 3373–3376. https://doi.org/10.1016/j.jmrt.2019.03.014.

Baczmański, A., Braham, C., 2004. Elastoplastic properties of duplex steel determined using neutron diffraction and self-consistent model. Acta Mater. 52, 1133–1142. https://doi.org/10.1016/j.actamat.2003.10.046.

Baczmański, A., Gaj, A., Le Joncour, L., Wroński, S., Francois, M., Panicaud, B., Braham, C., Paradowska, A.M., 2012. Study of stress localisation in polycrystalline grains using self-consistent modelling and neutron diffraction. Philos. Mag. 92, 3015–3035. https://doi.org/10.1080/14786435.2012.683542.

Baczmanski, A., Lipinski, P., Tidu, A., Wierzbanowski, K., Pathiraj, B., 2008. Quantitative estimation of incompatibility stresses and elastic energy stored in ferritic steel. J. Appl. Crystallogr. 41, 854–867. https://doi.org/10.1107/S0021889808023911.

Baczmański, A., Zhao, Y., Gadalińska, E., Le Joncour, L., Wroński, S., Braham, C., Panicaud, B., François, M., Buslaps, T., Soloducha, K., 2016. Elastoplastic deformation and damage process in duplex stainless steels studied using synchrotron and neutron diffractions in comparison with a self-consistent model. Int. J. Plast. 81, 102–122. https://doi.org/10.1016/j.ijplas.2016.01.018.
Basinski, Z.S., Hume-Rothery, W., Sutton, L., 1955. The lattice expansion of iron. Proc. R. Soc. Lond. Ser A Math. Phys. Sci. 229, 459–467. https://doi.org/10.1098/rspa.1955.0102.
Berveiller, M., Zaoui, A., 1978. An extension of the self-consistent scheme to plastically-flowing polycrystals. J. Mech. Phys. Solids 26, 325–344. https://doi.org/10.1016/0022-5096(78)90003-0.
Beyerlein, I.J., Tomé, C.N., 2008. A dislocation-based constitutive law for pure Zr including temperature effects. Int. J. Plast. 24, 867–895. https://doi.org/10.1016/j.ijplas.2007.07.017.
Bishop, J.F.W., Hill, R., 1951. XLVI. A theory of the plastic distortion of a polycrystalline aggregate under combined stresses. Lond. Edinb. Dublin Philos. Magaz. J. Sci. 42, 414–427. https://doi.org/10.1080/14786445108561065.
Bonfoh, N., Carmasol, A., Lipinski, P., 2003. Modeling of intra-crystalline hardening of materials with particles. Int. J. Plast. 19, 1167–1193. https://doi.org/10.1016/S0749-6419(02)00015-3.
Bonfoh, N., Lipinski, P., Carmasol, A., Tiem, S., 2004. Micromechanical modeling of ductile damage of polycrystalline materials with heterogeneous particles. Int. J. Plast. 20, 85–106. https://doi.org/10.1016/S0749-6419(03)00017-2.
Bouaziz, O., Buessler, P., 2004. Iso-work increment assumption for heterogeneous material behaviour modelling. Adv. Eng. Mater. https://doi.org/10.1002/adem.200300524.
Bouaziz, O., Le Corre, C., 2003. Flow stress and microstructure modelling of ferrite-pearlite steels during cold rolling. In: Materials Science Forum, pp. 1399–1404.
Cai, S., Daymond, M.R., Holt, R.A., 2012. Deformation of high β-phase fraction Zr-Nb alloys at room temperature. Acta Mater. 60, 3355–3369. https://doi.org/10.1016/j.actamat.2012.02.040.
Che, L., Gotoh, M., Horimoto, Y., Hirose, Y., 2007. Effect of microstructure of cementite on interphase stress state in carbon steel. J. Iron Steel Res. Int. 14, 31–38. https://doi.org/10.1016/S1006-706X(07)60054-5.
Chelladurai, I., Adams, D., Fullwood, D.T., Miles, M.P., Niezgoda, S., Beyerlein, I.J., Knezevic, M., 2019. Modeling of trans-grain twin transmission in AZ31 via a neighborhood-based viscoplastic self-consistent model. Int. J. Plast. https://doi.org/10.1016/j.ijplas.2018.03.012.
Cherkaoui, M., Sabar, H., Berveiller, M., 1994. Micromechanical approach of the coated inclusion problem and applications to composite materials. J. Eng. Mater. Technol. 116, 274–278. https://doi.org/10.1115/1.2904286.
Das, A., 2018. Calculation of ductility from pearlite microstructure. Mater. Sci. Technol. 34, 1046–1063. https://doi.org/10.1080/02670836.2017.1418476.
Daymond, M.R., Priesmeyer, H.G., 2002. Elastoplastic deformation of ferritic steel and cementite studied by neutron diffraction and self-consistent modelling. Acta Mater. 50, 1613–1626. https://doi.org/10.1016/S1359-6454(02)00026-5.
Dollar, M., Bernstein, I.M., Thompson, A.W., 1988. Influence of deformation substructure on flow and fracture of fully pearlitic steel. Acta Metall. 36, 311–320. https://doi.org/10.1016/0001-6160(88)90008-9.
Embury, J.D., Fisher, R.M., 1966. The structure and properties of drawn pearlite. Acta Metall. 14, 147–159. https://doi.org/10.1016/0001-6160(66)90296-3.
Eshelby, J.D., 2007. The determination of the elastic field of an ellipsoidal inclusion, and related problems, 241. Collect. Work. J. D. Eshelby, pp. 209–229. https://doi.org/10.1007/1-4020-4499-2_18.
Fajoui, J., Gloaguen, D., Legrand, V., Oum, G., Kelleher, J., Kockelmann, W., 2016. Bauschinger Effect in an Austenitic Steel: Neutron Diffraction and a Multiscale Approach. Metall. Mater. Trans. A Phys. Metall. Mater. Sci. 47, 2024–2036. https://doi.org/10.1007/s11661-016-3362-5.
Fang, F., Zhao, Y., Liu, P., Zhou, L., Hu, X. jun, Zhou, X., Xie, Z. han, 2014. Deformation of cementite in cold drawn pearlitic steel wire. Mater. Sci. Eng. A. https://doi.org/10.1016/j.msea.2014.04.050.
Franz, G., Abed-Meraim, F., Berveiller, M., 2013. Strain localization analysis for single crystals and polycrystals: Towards microstructure-ductility linkage. Int. J. Plast. 48, 1–33. https://doi.org/10.1016/j.ijplas.2013.02.001.
Gadalińska, E., Baczmański, A., Wroński, S., Kot, P., Wroński, M., Wróbel, M., Scheffzük, C., Bokuchava, G., Wierzbanowski, K., 2018. Neutron diffraction study of phase stresses in Al/SiCp composite during tensile test. Met. Mater. Int. https://doi.org/10.1007/s12540-018-00218-7. Evaliable on.
Ghosh, P., Kormout, K.S., Lienert, U., Keckes, J., Pippan, R., 2018. Deformation characteristics of ultrafine grained and nanocrystalline iron and pearlitic steel - an in situ synchrotron investigation. Acta Mater. 160, 22–33. https://doi.org/10.1016/j.actamat.2018.08.036.
Gloaguen, D., Fajoui, J., Girault, B., 2014. Residual stress fields analysis in rolled Zircaloy-4 plates: grazing incidence diffraction and elastoplastic self-consistent model. Acta Mater. 71, 136–144. https://doi.org/10.1016/j.actamat.2014.02.031.
Hammersley, A.P., Svensson, S.O., Hanfland, M., Fitch, A.N., Hausermann, D., 2007. Two-dimensional detector software: from real detector to idealised image or two-theta scan. High Press. Res. 14, 235–248. https://doi.org/10.1080/08957959608201408.
Hauk, V., 1997. Structural and Residual Stress Analysis by Nondestructive Methods. Institute of Materials, London, UK.
Hill, R., 1967. The essential structure of constitutive laws for metal composites and polycrystals. J. Mech. Phys. Solids 15, 79–95. https://doi.org/10.1016/0022-5096(67)90018-X.
Hill, R., 1965. A self-consistent mechanics of composite materials. J. Mech. Phys. Solids 13, 213–222. https://doi.org/10.1016/0022-5096(65)90010-4.
Hounkpati, V., Fréour, S., Gloaguen, D., Legrand, V., Kelleher, J., Kockelmann, W., Kabra, S., 2016. In situ neutron measurements and modelling of the intergranular strains in the near-β titanium alloy Ti-β21S. Acta Mater. 109, 341–352. https://doi.org/10.1016/j.actamat.2016.02.065.
Hutchinson, J.W., 1970. Elastic-plastic behaviour of polycrystalline metals and composites. Proc. R. Soc. A Math. Phys. Eng. Sci. https://doi.org/10.1098/rspa.1970.0177.
Iza-Mendia, A., Gutiérrez, I., 2013. Generalization of the existing relations between microstructure and yield stress from ferrite-pearlite to high strength steels. Mater. Sci. Eng. A 561, 40–51. https://doi.org/10.1016/j.msea.2012.10.012.
Jia, N., Cong, Z.H., Sun, X., Cheng, S., Nie, Z.H., Ren, Y., Liaw, P.K., Wang, Y.D., 2009. An in situ high-energy X-ray diffraction study of micromechanical behavior of multiple phases in advanced high-strength steels. Acta Mater. 57, 3965–3977. https://doi.org/10.1016/j.actamat.2009.05.002.
Kante, S., Leineweber, A., 2019. Two-phase and three-phase crystallographic relationships in white-solidified and nitrided Fe-C-Si cast iron. Acta Mater. 170, 240–252. https://doi.org/10.1016/j.actamat.2019.03.029.
Kot, P., Baczmański, A., Gadalińska, E., Wroński, S., Wroński, M., Wróbel, M., Bokuchava, G., Scheffzük, C., Wierzbanowski, K., 2019. Evolution of phase stresses in Al/SiCp composite during thermal cycling and compression test studied using diffraction and self-consistent models. J. Mater. Sci. Technol. accepted.
Kröner, E., 1961. Zur plastischen verformung des vielkristalls. Acta Metall. 9, 155–161.
Lamontagne, A., Massardier, V., Kléber, X., Sauvage, X., Mari, D., 2015. Comparative study and quantification of cementite decomposition in heavily drawn pearlitic steel wires. Mater. Sci. Eng. A 644, 105–113. https://doi.org/10.1016/j.msea.2015.07.048.
Langford, G., Cohen, M., 1969. Strain hardening of iron by severe plastic deformation. ASM-Trans. 62 (3), 623–638.
Lebensohn, R.A., Kanjarla, A.K., Eisenlohr, P., 2012. An elasto-viscoplastic formulation based on fast Fourier transforms for the prediction of micromechanical fields in polycrystalline materials. Int. J. Plast. 32–33, 59–69. https://doi.org/10.1016/j.ijplas.2011.12.005.
Ledbetter, H., 2010. Polycrystalline elastic constants of in situ cementite (Fe3C). Mater. Sci. Eng. A 527, 2657–2661. https://doi.org/10.1016/j.msea.2009.12.034.
Leitner, T., Hohenwarter, A., Pippan, R., 2019. Anisotropy in fracture and fatigue resistance of pearlitic steels and its effect on the crack path. Int. J. Fatigue 124, 528–536. https://doi.org/10.1016/j.ijfatigue.2019.02.048.
Li, S., Yip, T.H., Ramanujan, R.V., Liang, M.H., 2003. In situ TEM studies of the mechanisms of crack nucleation and propagation in fully lamellar microstructures. Mater. Sci. Technol. 19, 902–906. https://doi.org/10.1179/026708303225004378.
Li, Y., Raabe, D., Herbig, M., Choi, P.P., Goto, S., Kostka, A., Yarita, H., Borchers, C., Kirchheim, R., 2014. Segregation stabilizes nanocrystalline bulk steel with near theoretical strength. Phys. Rev. Lett. 113 https://doi.org/10.1103/PhysRevLett.113.106104.
Lin, T.H., 1971. Physical theory of plasticity. Adv. Appl. Mech. 11, 255–311. https://doi.org/10.1016/S0065-2156(08)70344-2.
Lin, T.H., 1957. Analysis of elastic and plastic strains of a face-centred cubic crystal. J. Mech. Phys. Solids. https://doi.org/10.1016/0022-5096(57)90058-3.

Linz, M., Rodríguez Ripoll, M., Pauly, C., Bernardi, J., Steiger-Thirsfeld, A., Franek, F., Mücklich, F., Gachot, C., 2018. Heterogeneous strain distribution and saturation of geometrically necessary dislocations in a ferritic-pearlitic steel during lubricated sliding. Adv. Eng. Mater. 20 https://doi.org/10.1002/adem.201700810.
Lipinski, P., Berveiller, M., 1989. Elastoplasticity of micro-inhomogeneous metals at large strains. Int. J. Plast. 5, 149–172. https://doi.org/10.1016/0749-6419(89)90027-2.
Lipinski, P., Berveiller, M., Reubrez, E., Morreale, J., 1995. Transition theories of elastic-plastic deformation of metallic polycrystals. Arch. Appl. Mech. https://doi.org/10.1007/BF00789222.
Liu, Y., Yang, C.D., Liu, M., Wang, C.H., Dai, Y.C., Li, X., Russell, A.M., Zhang, C.X., Zhang, Z.H., Cao, G.H., 2018. Effects of microstructure and crystallography on mechanical properties of cold-rolled SAE1078 pearlitic steel. Mater. Sci. Eng. A 709, 115–124. https://doi.org/10.1016/j.msea.2017.10.050.
Long, X., Peng, X., Pi, W., 2008. A microstructure-based analysis of cyclic plasticity of pearlitic steels with Hill's self-consistent scheme incorporating general anisotropic Eshelby tensor. Acta Mech. Sin. Xuebao 24, 91–99. https://doi.org/10.1007/s10409-007-0120-3.
Mandel, J., 1966. Contribution théorique à l'étude de l'écrouissage et des lois de l'écoulement plastique. In: Applied Mechanics, pp. 502–509. https://doi.org/10.1007/978-3-662-29364-5_67.
Marcadon, V., Herve, E., Zaoui, A., 2007. Micromechanical modeling of packing and size effects in particulate composites. Int. J. Solids Struct. 44, 8213–8228. https://doi.org/10.1016/j.ijsolstr.2007.06.008.
Marder, A.R., Bramfitt, B.L., 1976. The effect of morphology on the strength of pearlite. Metall. Trans. A 7, 365–372. https://doi.org/10.1007/BF02642832.
Merkel, S., Hilairet, N., 2015. Multifit/Polydefix: a framework for the analysis of polycrystal deformation using X-rays. J. Appl. Crystallogr. 48, 1307–1313. https://doi.org/10.1107/S1600576715010390.
Morawiec, A., 2004. Orientations and Rotations, Orientations and Rotations. Springer, Berlin, Heidelberg. https://doi.org/10.1007/978-3-662-09156-2.
Nakada, N., Koga, N., Tsuchiyama, T., Takaki, S., 2009. Crystallographic orientation rotation and internal stress in pearlite colony. Scr. Mater. 61, 133–136. https://doi.org/10.1016/j.scriptamat.2009.03.028.
Neil, C.J., Wollmershauser, J.A., Clausen, B., Tomé, C.N., Agnew, S.R., 2010. Modeling lattice strain evolution at finite strains and experimental verification for copper and stainless steel using in situ neutron diffraction. Int. J. Plast. 26, 1772–1791. https://doi.org/10.1016/j.ijplas.2010.03.005.
Nikolussi, M., Shang, S.L., Gressmann, T., Leineweber, A., Mittemeijer, E.J., Wang, Y., Liu, Z.K., 2008. Extreme elastic anisotropy of cementite, Fe3C: first-principles calculations and experimental evidence. Scr. Mater. 59, 814–817. https://doi.org/10.1016/j.scriptamat.2008.06.015.
Oliver, E.C., Daymond, M.R., Withers, P.J., 2004. Interphase and intergranular stress generation in carbon steels. Acta Mater. 52, 1937–1951. https://doi.org/10.1016/j.actamat.2003.12.035.
Reuss, A., 1929. Berechnung der Fließgrenze von Mischkristallen auf Grund der Plastizitätsbedingung für Einkristalle. ZAMM - J. Appl. Math. Mech./Z. Angew. Math. Mech. https://doi.org/10.1002/zamm.19290090104.
Sachs, G., 1928. Zur Ableitung einer Fliessbedinung. Zeitschrift des VDI 72, 734–736.
Shimokawa, T., Niiyama, T., Okabe, M., Sawakoshi, J., 2019. Interfacial-dislocation-controlled deformation and fracture in nanolayered composites: toward higher ductility of drawn pearlite. Acta Mater. 164, 602–617. https://doi.org/10.1016/j.actamat.2018.10.061.
Sidhom, H., Yahyaoui, H., Braham, C., Gonzalez, G., 2015. Analysis of the deformation and damage mechanisms of pearlitic steel by EBSD and "in-situ" SEM tensile tests. J. Mater. Eng. Perform. 24, 2586–2596. https://doi.org/10.1007/s11665-015-1537-7.
Simmons, G., Wang, H., 1971. Single Crystal Elastic Constants and Calculated Aggregate Properties: a Handbook. The MIT Press, Cambridge, London.
Taniyama, A., Takayama, T., Arai, M., Hamada, T., 2017. Deformation behavior of cementite in deformed high carbon steel observed by X-ray diffraction with synchrotron radiation. Metall. Mater. Trans. A Phys. Metall. Mater. Sci. 48, 4821–4830. https://doi.org/10.1007/s11661-017-4229-0.
Taupin, V., Pesci, R., Berbenni, S., Berveiller, S., Ouahab, R., Bouaziz, O., 2013. Lattice strain measurements using synchrotron diffraction to calibrate a micromechanical modeling in a ferrite-cementite steel. Mater. Sci. Eng. A 561, 67–77. https://doi.org/10.1016/j.msea.2012.10.086.
Taylor, G.I., 1938. Plastic strain in metals. J. Inst. Met. 62, 307–324 https://doi.org/not found.
Tome, C., Canova, G.R., Kocks, U.F., Christodoulou, N., Jonas, J.J., 1984. The relation between macroscopic and microscopic strain hardening in F.C.C. polycrystals. Acta Metall. 32, 1637–1653. https://doi.org/10.1016/0001-6160(84)90222-0.
Turner, P.A., Tomé, C.N., 1994. A study of residual stresses in Zircaloy-2 with rod texture. Acta Metall. Mater. 42, 4143–4153. https://doi.org/10.1016/0956-7151(94)90191-0.
Upadhyay, M.V., Patra, A., Wen, W., Panzner, T., Van Petegem, S., Tomé, C.N., Lebensohn, R.A., Van Swygenhoven, H., 2018. Mechanical response of stainless steel subjected to biaxial load path changes: Cruciform experiments and multi-scale modeling. Int. J. Plast. 108, 144–168. https://doi.org/10.1016/j.ijplas.2018.05.003.
Voigt, W., 1928. Lehrbuch der Kristallphysik, Lehrbuch der Kristallphysik. https://doi.org/10.1007/978-3-663-15884-4.
Wawszczak, R., Baczmański, A., Marciszko, M., Wróbel, M., Czeppe, T., Sztwiertnia, K., Braham, C., Berent, K., 2016. Evolution of microstructure and residual stress during annealing of austenitic and ferritic steels. Mater. Char. 112, 238–251. https://doi.org/10.1016/j.matchar.2015.12.019.
Wei, D., Li, L., Min, X., Fang, F., Xie, Z., Jiang, J., 2019. Microstructure and mechanical properties of heavily cold drawn pearlitic steel wires: effects of low temperature annealing. Mater. Char. 153, 108–114. https://doi.org/10.1016/j.matchar.2019.05.003.
Weisser, M.A., Evans, A.D., Van Petegem, S., Holdsworth, S.R., Van Swygenhoven, H., 2011. In situ room temperature tensile deformation of a 1% CrMoV bainitic steel using synchrotron and neutron diffraction. Acta Mater. 59, 4448–4457. https://doi.org/10.1016/j.actamat.2011.03.068.
Weisser, M.A., Van Petegem, S., Cervellino, A., Van Swygenhoven, H., 2015. On the origin of cementite diffraction peak broadening during tensile deformation at ambient temperatures. Int. J. Plast. 66, 138–144. https://doi.org/10.1016/j.ijplas.2014.10.008.
Wroński, S., Baczmański, A., Dakhlaoui, R., Braham, C., Wierzbanowski, K., Oliver, E.C., 2007. Determination of the stress field in textured duplex steel using the TOF neutron diffraction method. Acta Mater. 55, 6219–6233. https://doi.org/10.1016/j.actamat.2007.07.044.
Xiang, L., Liang, L.W., Wang, Y.J., Chen, Y., Wang, H.Y., Dai, L.H., 2019. One-step annealing optimizes strength-ductility tradeoff in pearlitic steel wires. Mater. Sci. Eng. A 757, 1–13. https://doi.org/10.1016/j.msea.2019.04.086.
Yahyaoui, H., Sidhom, H., Braham, C., Baczmanski, A., 2014. Effect of interlamellar spacing on the elastoplastic behavior of C70 pearlitic steel: experimental results and self-consistent modeling. Mater. Des. 55, 888–897. https://doi.org/10.1016/j.matdes.2013.10.062.
Young, M.L., Almer, J.D., Daymond, M.R., Haeffner, D.R., Dunand, D.C., 2007. Load partitioning between ferrite and cementite during elasto-plastic deformation of an ultrahigh-carbon steel. Acta Mater. 55, 1999–2011. https://doi.org/10.1016/j.actamat.2006.11.004.
Zhang, X., Godfrey, A., Hansen, N., Huang, X., 2013. Hierarchical structures in cold-drawn pearlitic steel wire. Acta Mater. 61, 4898–4909. https://doi.org/10.1016/j.actamat.2013.04.057.
Zhang, X., Hansen, N., Godfrey, A., Huang, X., 2018. Structure and strength of sub-100 nm lamellar structures in cold-drawn pearlitic steel wire. Mater. Sci. Technol. 34, 794–808. https://doi.org/10.1080/02670836.2018.1440155.
Zhang, Y.D., Esling, C., Calcagnotto, M., Zhao, X., Zuo, L., 2007. New insights into crystallographic correlations between ferrite and cementite in lamellar eutectoid structures, obtained by SEM-FEG/EBSD and an indirect two-trace method. J. Appl. Crystallogr. 40, 849–856. https://doi.org/10.1107/S0021889807032219.
Zhao, Y., Tan, Y., Ji, X., Xiang, Z., He, Y., Xiang, S., 2018. In situ study of cementite deformation and its fracture mechanism in pearlitic steels. Mater. Sci. Eng. A 731, 93–101. https://doi.org/10.1016/j.msea.2018.05.114.
Zhou, D.S., Shiflet, G.J., 1992. Ferrite: cementite crystallography in pearlite. Metall. Trans. A 23, 1259–1269. https://doi.org/10.1007/BF02665057.